arXiv:1511.06500v1 [astro-ph.SR] 20 Nov 2015

Achieving Consistent Doppler Measurements from *SDO*/HMI Vector Field Inversions

Peter W. Schuck[1]

peter.schuck@nasa.gov

Spiro Antiochos[2]

spiro.antiochos@nasa.gov

and

K. D. Leka[3]

leka@cora.nwra.com

and

Graham Barnes[3]

graham@cora.nwra.com

Received _____; accepted _____

Submitted to ApJ

[1]Space Weather Laboratory, Code 674, Heliophysics Science Division, NASA Goddard Space Flight Center 8800 Greenbelt Rd. Greenbelt, MD 20771

[2]Heliophysics Science Division NASA Goddard Space Flight Center 8800 Greenbelt Rd. Greenbelt, MD 20771

[3]NorthWest Research Associates 3380 Mitchell Lane Boulder, CO 80301

ABSTRACT

NASA's *Solar Dynamics Observatory* is delivering vector field observations of the full solar disk with unprecedented temporal and spatial resolution; however, the satellite is in a highly inclined geostationary orbit. The relative spacecraft-Sun velocity varies by ±3 km/s over a day which introduces major orbital artifacts in the Helioseismic Magnetic Imager data. We demonstrate that the orbital artifacts contaminate all spatial and temporal scales in the data. We describe a newly-developed three stage procedure for mitigating these artifacts in the Doppler data derived from the Milne-Eddington inversions in the HMI Pipeline. This procedure was applied to full disk images of AR11084 to produce consistent Dopplergrams. The data adjustments reduce the power in the orbital artifacts by 31dB. Furthermore, we analyze in detail the corrected images and show that our procedure greatly improve the temporal and spectral properties of the data without adding any new artifacts. We conclude that this new and easily implemented procedure makes a dramatic improvement in the consistency of the HMI data and in its usefulness for precision scientific studies.

Subject headings: methods: data analysis, instrumentation: polarimeters, Sun: granulation, Sun: helioseismology, Sun: magnetic fields

1. Introduction

The Helioseismic Magnetic Imager (HMI) aboard NASA's *Solar Dynamics Observatory* (*SDO*) produces full-sun vector magnetic field observations at 1″ resolution with a cadence of approximately 12 minutes. These data represent an unprecedented opportunity to study time evolution of solar vector magnetic fields on the spatial scales and time scales of active region evolution. For the first time relatively pristine data are available that are uncontaminated by the Earth's atmospheric seeing, which causes distortions that often cannot be completely corrected by speckle reconstruction imaging or adaptive optics. In principle, the HMI data can lead to major advances in science understanding, because the energy and helicity transported though the photosphere and into the corona can be determined by measuring plasma velocities (optical flow/image motions) from a sequence of vector magnetograms Schuck (2005, 2006, 2008). While speckle reconstruction imaging and adaptive optics can dramatically improve the local resolution of the images, these techniques often do not preserve the relative distances between solar structures from frame to frame which introduces large artificial biases in velocity estimates. In contrast, *SDO* represents a stable platform with a known pointing, located outside Earth's atmosphere, thereby potentially permitting highly accurate measurements of the velocities between photospheric features from frame to frame.

SDO, however, is in a highly inclined geosynchronous orbit chosen so as to maximize data throughput to the ground based receiving stations. Unfortunately, this orbit produces a large ±3 km/s variation in the relative velocity between the HMI instrument and the Sun, which leads to major orbital artifacts in the HMI data. Since the orbit is accurately known, it would seem that removal of the artifacts should be straightforward; but, even after five years into the mission, the exact mechanisms that contaminate the data remain a mystery and the rigorous removal of the artifacts has not been accomplished. There is speculation

that the artifacts are caused by the motion of the Fe I $\lambda_0 = 6173.343\,\text{Å}$ line across the HMI transmission filters as the satellite executes its geosynchronous orbit. Over the period of an orbit the radial velocity of the satellite varies by as much as ± 3.2 km/s, which corresponds to a shift of $\Delta\lambda \simeq \lambda_0\, 2\,\Delta v/c \simeq 131\,\text{mÅ}$, which is larger than the nominal HMI filter separation of $\Delta\lambda \simeq 69\,\text{mÅ}$. It is now well established that these artifacts contaminate many observables computed from HMI data (*e.g.*, Section 7.1 in Hoeksema et al. (2014), Fig. 4 in Liu & Schuck (2012) for AR11072 shows oscillations in the shear helicity flux, Fig. 3 in Chintzoglou & Zhang (2013) exhibits clear dips in the magnetic field near midnight on 14 Feb, 15 Feb and 16 Feb, and the Poynting flux in Fig. 2 of Vemareddy (2015) shows a very clear 12 hr oscillation). The optimal solution would be to understand the source of the contamination at the spectral level and correct optical distortions though calibration prior to any inversion process to estimate Doppler velocities and magnetic fields. However, even if the source of the contamination is definitively identified and corrected for future observations, it is unclear whether these corrections could be implemented for the data already archived. If the HMI data are ever to be used for high-precision unbiased studies or for data-driven modeling, it is absolutely essential that a rigorous procedure be developed for mitigating the systematic errors in the archived and future data.

In this paper we present a new approach COADRED: Cleansing Orbital Artifacts – Demodulation by REnormalizing Data for correcting the down-stream Doppler velocities derived from the Milne-Eddington inversions. It should be emphasized that all spatial and temporal scales are affected by the artifacts, thereby rendering the data essentially useless for detailed quantitative spatio-temporal analysis at the cadence of the data series. The goal of our procedure describe below is to provide a data set that is consistent, i.e., free of orbital artifacts. Note that we cannot claim to derive data that are absolutely correct, because there are no absolute calibrations for the measurements. Potentially inter-calibration between vector magnetographs could determine which measurements are

correct, but presently there are no absolutely calibrated magnetographs to compare with. Furthermore, even understanding the relative calibrations between magnetographs is rife with complexities, because magnetograms often use different magnetically sensitive lines corresponding to different heights in the solar atmosphere, with different spatial resolutions, different spectral sampling, and different time-cadence (Leka & Steiner 2001; Leka et al. 2009; Orozco Suárez et al. 2007; Leka 2011; Leka et al. 2012; Leka & Barnes 2012). Given these many obstacles to determining absolute calibrations for the purposes of "correcting" any of the observables from the HMI Pipeline data we focus our attention instead on producing *artifact-free, consistent* data by renormalizing the observables to the rest velocity of the satellite $V_{\rm R} \rightarrow 0$. We emphasize that even the measurements observed at $V_{\rm R} = 0$ may not be "correct" in an absolute sense. Indeed, we will show that significant biases remain. However, this renormalization does remove most of the contamination correlated with the spacecraft orbital velocity. The result is a rigorous consistent data that can now be used for spatio-temporal analysis of the image dynamics.

1.1. The COADRED Procedure

COADRED consists of a three stage process for obtaining consistent Doppler measurements[1] with vector field data from the HMI Pipeline.

1. The first step is to remove the projection of the satellite velocity along the line-of-sight (LOS) from each pixel. Since the satellite orbit is known with high accuracy, then in principle, if the HMI measurements were precise, there would be no orbital effects remaining in the data. As will be shown below, however, this is definitely not the case.

2. We next remove the three well-known quasi steady-state signals from each image: the

[1] Specifically the hmi.ME_720s_fd10{vlos_mag} data.

differential rotation, the meridional flows, and the convective blue-shift. Note that the first two are actual physical flows, but the latter is not. As discussed in detail by Beckers & Nelson (1978), the convective blue-shift, commonly referred to as the limb shift, is due to the observed strong correlation in photospheric lines between intensity and wavelength shift. For unresolved convective flows this correlation introduces a systematic bias to any line shift determinations, and this bias has a strong center-to-limb variation. The three large-scale signals are removed by fitting each image with a series of eigenfunctions representing the differential rotation, the meridional flows, and the limb shift "flows", and subtracting these from each image. Not surprisingly, these biases vary with *SDO*'s orbital velocity, and thus by removing them from each image, we reduce the power in the orbital effects substantially. We find that a low order, ~ 8, series for each type of flow is sufficient for fitting and removing the large-scale biases.

3 After removal of these biases, we expect that the only remaining physical effects in the residual images are the small-scale convective dynamics, which should be largely quasi-stationary. However we show below that these residual images still exhibit substantial orbital artifacts. We conjecture that these artifacts are caused by some type of interference between the instrument response and convective structures moving across the solar disk, which produces spectral artifacts by spatio-temporal modulation of the convective amplitudes. If so, then we expect there to be a strong correlation of *SDO*'s radial velocity with the limb shift effect in the instrument response. To remove this artifact, we calculate the magnitude of each residual image and then fit this with an eighth-order series of limb shift eigenfunctions. This yields the dependence of the coefficients on the satellite radial velocity $V_{\rm R}$. As will be shown below, the coefficients exhibit a clear systematic dependence with $V_{\rm R}$, which must be due to orbital artifacts. Consequently, we simply renormalize each pixel so that each image appears to be observed at the same orbital velocity, *arbitrarily* chosen in this case, to be $V_{\rm R} \equiv 0$. This renormalization almost completely eliminates

the orbital signal, so then we simply add back in the large-scale flows to obtain HMI Dopplergrams that exhibit essentially no orbital artifacts and that now can be used for accurate science investigations.

In the Sections below we describe the data set that we used for this analysis and describe exactly how the COADRED procedure was applied to this data set. The data and the procedure are described in sufficient detail that others can use our methods or can modify them for application to other types of data sets.

2. Data Description

Approximately 17 days of *SDO*/HMI data in 2010 are considered in developing the COADRED procedure. During this time period, the Sun was fairly quiet but these days encompass the disk passage of the small and nearly potential active region 11072 discussed by Liu & Schuck (2012). This time-period was specifically chosen for two reasons. First, it was relatively quiet period, and therefore most pixels represented the same physical process of solar convection. This permitted the straight-forward disentanglement of the orbital effects and the physical solar effects. Second, there was coverage by both HMI and MDI during this time.

The HMI has two independent cameras that produce several data series, which undergo different analysis. Consequently, these data sets may be used to inter-compare observations of the Sun. Three data series are produced by the vector field "side camera" (Keyword CAMERA=1). The hmi.M_720s{Magnetogram} and hmi.V_720s{Dopplergram} series are produced by an MDI-like algorithm (Couvidat et al. 2012) and the hmi.ME_720s_fd10 series with segments {field, azimuth, inclination, vlos_mag, etc} (Hoeksema et al. 2014) which are produced by the Very Fast Inversion of the Stokes Vector (VFISV, Borrero et al. 2009;

Centeno et al. 2014) Milne-Eddington code. Two data series are produce by the Doppler Camera (Keyword CAMERA=2) hmi.M_45s{magnetogram} and hmi.M_45s{Dopplergram} (Schou et al. 2012; Scherrer et al. 2012; Hoeksema et al. 2014). These four series have corrections and calibrations that are not applied to the spectral data provided to the Mile-Eddington inversions which are part of the hmi.ME_720s_fd10 series with segments {field, azimuth, inclination, vlos_mag, etc, etc} (Hoeksema et al. 2014). Furthermore, during 2010 there was a significant period of overlap in the observing programs of HMI and MDI. The MDI instrument produces two series which are comparable to observables estimated by HMI namely mdi.fd_M_96m_lev182 which is a LOS magnetogram and mdi.fd_V which is a LOS Dopplergram. Thus, in principle, there are three independent cameras and 4 different data sets for each LOS observable available for inter-comparison for AR11084. This paper will focus on the hmi.ME_720s_fd10{vlos_mag} data which with vector field "side camera" which measures 4096x4096 filtergrams at six wavelengths and four polarizations of the Fe I 617.3 nm line which are corrected for solar rotation, cosmic rays, distortions and other effects (Hoeksema et al. 2014). These spectral data are used to construct the Stokes parameters (I,Q,U,V) which are in turn inverted based on the Milne-Eddington approximations using VFISV (Very Fast Inversion of the Stokes Vector) to produce about 10 physical parameters including the magnetic components relative to the line of sight $\boldsymbol{B}_\xi$, $\boldsymbol{B}_\eta$, $\boldsymbol{B}_\zeta$ and the magnetized plasma velocity along the line of sight $v_{\rm LOS}$. Since the data are spectrally sparse and the Milne-Eddington model is a simplified description of the line-forming physics, the inversion of these spectra is highly sensitive to the relative velocity between the instrument and the line forming region on the Sun.

2.1. Camera#1 Orientation

The pointing of HMI is known to very high accuracy due to the Venus transit data of June 5-6, 2012 (Couvidat 2014; Emilio et al. 2015). In particular, The CROTA2 keyword is often taken to be the orientation of the Sun's North pole in Solar images. However, this interpretation depends specifically on how CROTA2 is determined. For HMI, the CROTA2 keywords is known to better than 0.002° (Couvidat 2014) *relative to the transit of Venus*. We caution the reader that this is not an absolute determination relative to the Sun's North Pole either relative to magnetic phenomena or solar flows. Furthermore, the P-angle and B0-angle estimates in the HMI Pipeline keywords do not include the corrections to the Carrington elements determined by Beck & Giles (2005) using time-distance helioseismology on data from *SOHO*/MDI. Beck & Giles (2005) found that Carrington's estimates of i the angle between the plane of the ecliptic and the solar equator, and Ω the angle between the cross point of the solar equator with the ecliptic and the vernal equinox were off by as much as $\Delta i = 0.095 \pm 0.002°$ and $\Delta\Omega = -0.17 \pm 0.1°$ with the error in i effecting the error in P-angle and CROTA2 more than the error in Ω. This may introduce a temporal error in CROTA2 of as much as 0.1° depending on the heliocentric ecliptic longitude of the *SDO*. Furthermore, Beck & Giles (2005) concluded that the cross equatorial flow they measured could correspond to a systematic bias in P-angle of another $\simeq 0.1°$ under the assumption that the Sun does not maintain long term cross equatorial flows. These results suggest that generally there may be a time-dependent error in the inferred direction of Solar North of as much as $\simeq 0.2 - 0.3°$ when using the standard Carrington elements (This is not an HMI specific statement). Knowing these systematics is important for interpreting meridional flows as we shall see in Section 3.2.

Figure 1 shows the relative angle between HMI Camera#1 and MDI based on the normalized cross-correlation of the mdi.fd_M_96m_lev182 and the hmi.M_720s series

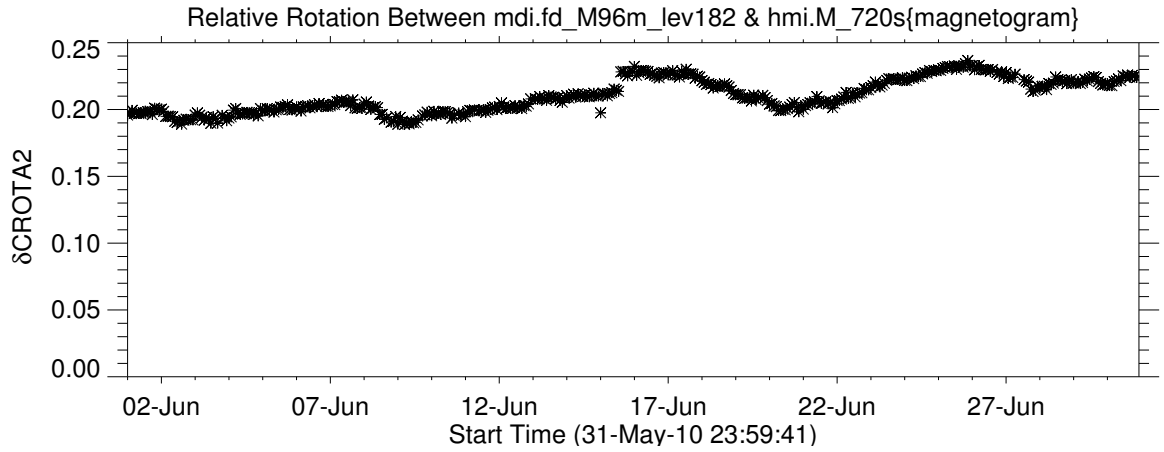

Fig. 1.— Relative roll-angle between HMI Camera#1 and MDI based on the hmi.M_720s series.

during the 2010 June. The MDI series keywords CRVAL1 and CRVAL2 were adjusted by 1.9 and -0.5 respectively to maximize the cross-correlation coefficient $C \simeq 0.9$ for the results presented here. The MDI image was convolved with a Gaussian filter, $\sigma_{\rm MDI} = 1$ pixel, and the HMI image was convolved with $\sigma_{\rm HMI} = 4 \times 0.875 = 3.5$ pixels, chosen to maximize the cross-correlation. Convolving both data sets with a Gaussian reduces shot noise. The CROTA2 value for the HMI image was then adjusted by CROTA2 $\rightarrow$ CROTA2 $-$ δCROTA2 over a range of -1° to 1° where positive δCROTA2 corresponds to a counterclockwise(clockwise) rotation of HMI(MDI) to bring them into alignment. The Carrington/Stonyhurst coordinates were used to determined the same locations on each image and the blurred HMI image was re-sampled to MDI observations. The offset between the two cameras lies between 0.18° and 0.23°. The variation could be due to a drift in CRPIX or roll in MDI. At present, there is no predictive or definitive attitude data for SOHO during this time period,[2] but these values are in rough agreement

[2]`http://sohowww.nascom.nasa.gov/data/ancillary/#attitude`

with Liu et al. (2012) who found $\delta\mathrm{CROTA2} \simeq 0.22 - 0.10 = 0.12^\circ \pm 0.05^\circ$ in a comparison between the same two data series using a slightly different procedure. These results imply that a CROTA2 value of 180 corresponds closely to solar North pointing downward in the images to within a few tenths of a degree.

2.2. Co-Registration

Figure 2 shows the radius of the Sun as observed by HMI over the 17 day period. On the time scale of a day, the diameter(radius) of the Sun varies by roughly $1''\,(0.5'')$ corresponding to roughly two pixels and on the time-scale of 17 days the diameter(radius) of the Sun varies by roughly $2''\,(1'')$ corresponding to roughly four pixels. For spatio-temporal analysis, the optimal solution would be to track the active region across the Sun at the average speed of the active region. However, non-uniformities in the HMI instrument response then convolve noise in space and time (see movies). The Co-registration choice for this investigation is to: (1) shift each image so that the center of the Sun corresponds to the center of the image ($\mathrm{CRPIX1} = 2048.5, \mathrm{CRPIX2} = 2048.5$), (2) rotate each image to the same orientation ($\mathrm{CROTA2} = 0$), and remap each image to the same observation point DSUN_OBS = 152017949201 m (distance to the Sun), so that the solar radius remains constant in pixel units. Using this co-registration convention each pixel corresponds to the same nominal location on the solar disk.

3. Doppler Data Processing

The following sections describe the exact procedure by which the HMI data are processed in order to remove the orbital artifacts. In the subsequent analysis the variable U is used to represent components of a velocity on the surface of the Sun and and the variable

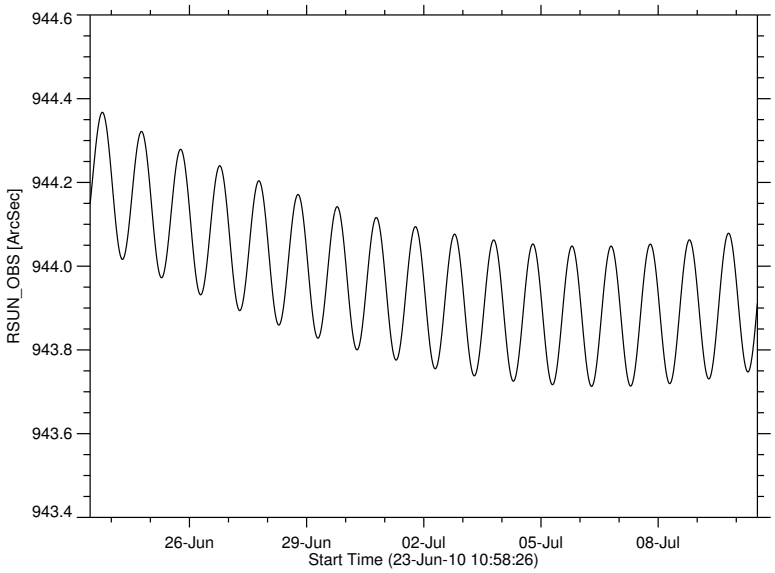

Fig. 2.— The radius of the Sun in arc-seconds as observed by *SDO*/HMI. Since the resolution of each pixel is fixed in the images, this implies that the effective solar radius in pixel units is varying from image-to-image in the hmi.ME_720s_fd10 series as *SDO* orbits the earth.

$\boldsymbol{V}_{SDO}$ is used the spacecraft velocity, but generally $\mathcal{V}$ is used to represent a theoretical model of the line-of-sight (LOS) Doppler velocity and $v_{\rm LOS}$ is used to represent various stages of data processing $v_{\rm LOS-0}$, $v_{\rm LOS-1}$, $v_{\rm LOS-2}$, and $v_{\rm LOS-3}$ with $v_{\rm LOS-0}$ representing the raw observed Doppler velocity form the HMI Pipeline. The coordinate systems used are described in the Appendices based on the notation in Thompson (2006). In particular, Appendix B describes the projection of the Stonyhurst unit vector $\left(\widehat{\boldsymbol{\Phi}}, \widehat{\boldsymbol{\Theta}}, \widehat{\boldsymbol{r}}\right)$ onto the LOS.

3.1. Stage 1: Subtraction of the LOS Projection of Satellite Velocity

The first stage in the analysis is the removal of the LOS projection of the satellite velocity (Sat-V) from each pixel. The Heliocentric-Cartesian LOS direction $(\widehat{\boldsymbol{x}}, \widehat{\boldsymbol{y}}, \widehat{\boldsymbol{z}})$ in

helioprojective coordinates (θ_ρ, ψ) is (See Appendix A)

$$\widehat{\boldsymbol{\eta}}_{\mathbf{LOS}}\,(\theta_\rho, \psi) = \sin\theta_\rho\,\sin\psi\,\widehat{\boldsymbol{x}} - \sin\theta_\rho\,\cos\psi\,\widehat{\boldsymbol{y}} + \cos\theta_\rho\,\widehat{\boldsymbol{z}}. \tag{A2}$$

Positive values of Doppler shift correspond to (redshifts) motion away from the satellite.[3] In principle, the LOS plasma motion on the Sun can be determined by subtracting the projection of the satellite motion onto the LOS from the measured Doppler velocity at each pixel

$$v_{\text{LOS–1}} = v_{\text{LOS–0}} - \widehat{\boldsymbol{\eta}}_{\mathbf{LOS}} \cdot \boldsymbol{V}_{SDO} \equiv -\widehat{\boldsymbol{\eta}}_{\mathbf{LOS}} \cdot \boldsymbol{U}_{\text{surface}}. \tag{A3b}$$

The velocity vector for *SDO* in the heliocentric Cartesian directions is

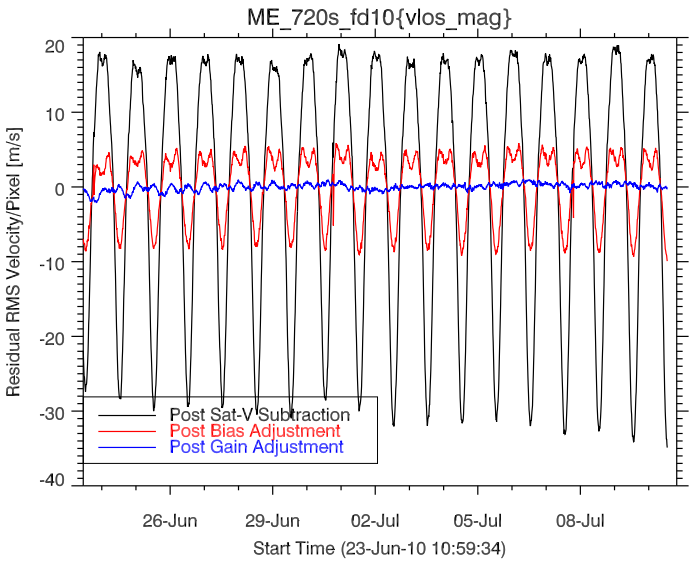

Fig. 3.— Residual spatially averaged RMS Doppler velocity during 17 days in 2010. (Black) after the projection of the satellite velocity has been removed from each pixel. (Red) after solar rotation V_{Rot}, meridional flows V_{MF}, and limb shift V_{LS}, have been removed.

[3] `http://jsoc.stanford.edu/doc/data/hmi/sharp/old/sharp.MB.htm`

$$\boldsymbol{V}_{SDO} = (V_{\rm W}, V_{\rm N}, V_{\rm R})\,, \tag{1a}$$

$$= (\text{OBS_VW}, \text{OBS_VN}, \text{OBS_VR})\,, \tag{1b}$$

in the Heliographic Cartesian coordinate system and thus

$$\widehat{\boldsymbol{\eta}}_{\mathbf{LOS}} \cdot \boldsymbol{V}_{SDO} = \text{OBS_VW} \sin\theta_\rho \sin\psi - \text{OBS_VN} \sin\theta_\rho \cos\psi + \text{OBS_VR} \cos\theta_\rho. \tag{2}$$

Here $V_{\rm R}$ corresponds to the HMI keyword "OBS_VR" which is the velocity of the observer in radial direction (positive is away from Sun). Additionally $V_{\rm W}$ corresponds to the the HMI keyword "OBS_VW" which is the velocity of the observer solar-westward (positive in the rough direction of Earth orbit), and $V_{\rm N}$ corresponds to "OBS_VN" which is the velocity of the observer solar-westward (positive in the direction of solar north).

If the Doppler velocities are measured accurately, the $v_{\rm LOS–1}$ would show no correlation with satellite motion. The black line in Figure 3 shows the residual spatially averaged RMS Doppler velocity

$$\text{Residual} = \left\langle \Delta \boldsymbol{v}^2_{\rm LOS} \right\rangle_x - \left\langle \Delta \boldsymbol{v}^2_{\rm LOS} \right\rangle_{x,t}\,, \tag{3}$$

during 17 days in 2010 after the projection of the satellite velocity has been subtracted from each pixel via (A3b). The subscripts "x" and "t" indicate spatial and temporal averaging respectively. A large, daily oscillation remains indicating *systematic* errors in the LOS Doppler measurements from the vector field inversions. Similar oscillations are known to occur in the B from the vector field inversions (see Hoeksema et al. 2014) and in the hmi.V_720s{Dopplergram} series from the same camera and in the 45 s cadence data from the hmi.V_45s series observed by camera 2 (private communication with Phil Scherrer). This strong fixed oscillation convolves with and pollutes all spatial and temporal scales, which greatly diminishes the usefulness of the data for science studies.

3.2. Stage 2: Large Scale Biases

The second stage in the COADRED procedure is the decomposition of each Doppler image into large-scale flows: differential rotation flows $\mathcal{V}_{\rm MF}$, meridional flows $\mathcal{V}_{\rm MF}$, and the convective blue-shift (limb shift) component $\mathcal{V}_{\rm LS}$. This determines an effective "bias" for each image according to

$$\mathcal{V}_{\rm bias} = \mathcal{V}_{\rm Rot}\left(B_0, \Phi, \Theta\right) + \mathcal{V}'_{\rm LS}\left(\varrho\right) + \mathcal{V}'_{\rm MF}\left(B_0, \Phi, \Theta\right), \tag{4}$$

where Φ and Θ are the Stonyhurst coordinates (Thompson 2006), B_0 is the so-called "Solar-B" angle, and ϱ is the heliocentric angle between the observer and the observed point (See Appendix C). The form of (2) and (A3b) suggests that artifacts introduced by the observer's radial velocity will project onto the limb shift functions (cylindrical symmetry), artifacts introduced by the observer's westward velocity will project onto the differential rotation profile, and artifacts introduced by the observer's northward velocity will project onto the meridional flow profile. Because the geosynchronous orbit of *SDO* causes significant changes in the radial velocity $V_{\rm R}$ over the period of a day, we conjecture that the projection of the radial velocity onto the limb shift functions is the most significant source of orbital artifacts in Dopplergrams. Consequently, step 3 of the procedure consists of a model for removing this effect, but first we must determine and subtract the known biases from the each image. The following three sections describe the standard mathematical formulation for capturing the differential rotation, meridional flow, and the limb shift "velocity." We then discuss, in detail, our application of this formalism to the HMI data.

3.2.1. Rotational Velocity

Following Hathaway (1988) the solar differential rotational velocity is decomposed by

$$U_\Phi^0\left(\Theta\right) = \sum_{\ell=1}^{\ell_{\max}} T_\ell^0 \, \sqrt{\ell \, \left(\ell+1\right)} \, \overline{\mathrm{P}}_\ell^1\left(\sin\Theta\right) \tag{5}$$

where

$$\overline{\mathrm{P}}_\ell^m\left(x\right) = \left(-1\right)^m \, \sqrt{\frac{\left(2\,\ell+1\right) \, \left(\ell-m\right)!}{2 \, \left(\ell+m\right)!}} \, \mathrm{P}_\ell^m\left(x\right), \tag{6}$$

and where P_ℓ^m are the associated Legendre functions[4]

$$\int_{-1}^{1} dx \, \mathrm{P}_k^m\left(x\right) \, \mathrm{P}_\ell^m\left(x\right) = \frac{2 \, \left(\ell+m\right)!}{\left(2\,\ell+1\right) \, \left(\ell-m\right)!} \, \delta_{k,\ell}. \tag{7}$$

Note that (6) leads to the definition of the spherical harmonics,

$$Y_\ell^m\left(\theta,\phi\right) = \left(-1\right)^m \, \sqrt{\frac{\left(2\,\ell+1\right)}{4\,\pi} \, \frac{\left(\ell-m\right)!}{\left(\ell+m\right)!}} \, \mathrm{P}_\ell^m\left(\cos\theta\right) \, e^{i\,m\,\phi} \equiv \overline{\mathrm{P}}_\ell^m\left(\cos\theta\right) \, \frac{e^{i\,m\,\phi}}{\sqrt{2\,\pi}}. \tag{8}$$

Using (A2), the projection of this solar differential rotation velocity onto the LOS velocity is then

$$\mathcal{V}_{\mathrm{Rot}}\left(B_0,\Phi,\Theta\right) = -\widehat{\boldsymbol{\eta}}_{\mathbf{LOS}} \cdot \boldsymbol{\mathcal{J}}^{\mathrm{T}} \cdot \widehat{\boldsymbol{\Phi}} \, U_\Phi^0\left(\Theta\right) \tag{9}$$

where for $\theta_\rho \approx 0$

$$\widehat{\boldsymbol{\eta}}_{\mathbf{LOS}} \cdot \boldsymbol{\mathcal{J}}^{\mathrm{T}} \cdot \widehat{\boldsymbol{\Phi}} \approx -\cos B_0 \, \sin\Phi. \tag{10}$$

The coefficients T_ℓ^0 are related to the usual A, B, C coefficients in

$$\omega\left(\Theta\right) = A + B \, \sin^2\Theta + C \, \sin^4\Theta = \frac{1}{R_\odot \, \cos\Theta} \sum_{\ell=1}^{\ell_{\max}} T_\ell^0 \, \sqrt{\ell \, \left(\ell+1\right)} \, \overline{\mathrm{P}}_\ell^1\left(\sin\Theta\right) \tag{11}$$

---

[4]as in Mathematica® and Interactive Data Language (IDL)®.

by

$$A = \frac{1}{16}\left(8\sqrt{6}\,T_1^0 - 12\sqrt{14}\,T_3^0 + 15\sqrt{22}\,T_5^0\right), \tag{12a}$$

$$B = \frac{15}{8}\left(2\sqrt{14}\,T_3^0 - 7\sqrt{22}\,T_5^0\right), \tag{12b}$$

$$C = \frac{315}{8}\sqrt{\frac{11}{2}}\,T_5^0. \tag{12c}$$

where $R_\odot = 6.95946^8$ km is the radius of the Sun for HMI (Emilio et al. 2015).

3.2.2. Limb Shift Velocity

Following Snodgrass (1984) and Hathaway (1992, 1996) the convective blue-shift, caused by correlations between velocity and intensity in unresolved convective elements (Beckers & Nelson 1978), is decomposed as

$$\mathcal{V}'_{\rm LS}(\varrho) = \sum_{\ell=0}^{N_{LS}} L_\ell\,(2\,\ell+1)^{-1/2}\,\mathcal{L}_\ell(1-\cos\varrho), \tag{13a}$$

where ϱ is the heliocentric angle between the observer and the observed point as defined in Appendix C, and

$$\mathcal{L}_n(x) = \sqrt{2}\,\overline{\rm P}_\ell^0(2\,x-1), \tag{13b}$$

are shifted Legendre polynomials orthonormal on $(0,1)$. A prime is used on (13a) to indicate that this is an adjusted limb shift function for reasons that will become apparent below.

3.2.3. Meridional Velocity

Again, following Hathaway (1992, 1996), the meridional flows are decomposed as

$$U_\Theta^0(\Theta) = \sum_{\ell=1}^{\ell_{\rm max}} S_\ell^0\,\sqrt{\ell\,(\ell+1)}\,\overline{\rm P}_\ell^1(\sin\Theta), \tag{14}$$

where positive coefficients correspond to northward velocities. In principle the projection of the meridional flows is given by

$$\mathcal{V}_{\rm MF}\left(B_0,\Phi,\Theta\right) = -\widehat{\boldsymbol{\eta}}_{\mathbf{LOS}}\cdot\boldsymbol{\mathcal{J}}^{\rm T}\cdot\widehat{\boldsymbol{\Theta}}\,U^0_\Theta\left(\Theta\right). \tag{15}$$

However Hathaway (1988) noticed that the meridional flow given by (14) has a projection onto the limb shift eigenfunctions. Thus, to orthogonalize the description of the large scale flows, this projection must be subtracted from the meridional flow eigenfunctions as it is already been accounted for in the limb shift eigenfunctions. Thus, the actual meridional flow description used to fit each image at stage 1 is given by

$$\mathcal{V}'_{\rm MF}\left(B_0,\Phi,\Theta\right) = -\sum_{\ell=1}^{\ell_{\rm max}} S^0_\ell\,\sqrt{\ell\,\left(\ell+1\right)}\,\left[\widehat{\boldsymbol{\eta}}_{\mathbf{LOS}}\cdot\boldsymbol{\mathcal{J}}^{\rm T}\cdot\widehat{\boldsymbol{\Theta}}\,\overline{\rm P}^1_\ell\left(\sin\Theta\right) - G_{{\rm MF},\ell}\left(B_0,\varrho\right)\right], \tag{16}$$

where

$$G_{{\rm MF},\ell}\left(B_0,\varrho\right) = \frac{1}{2\,\pi}\int_0^{2\,\pi} d\psi\,\widehat{\boldsymbol{\eta}}_{\mathbf{LOS}}\cdot\boldsymbol{\mathcal{J}}^{\rm T}\cdot\widehat{\boldsymbol{\Theta}}\,\overline{\rm P}^1_\ell\left(\sin\Theta\right), \tag{D1}$$

represents the spatial part of the meridional eigenfunction that is independent of position angle ψ. Indeed, (D1) is proportional to the meridional eigenfunction averaged over the position angle ψ. The integral in (D1) requires some effort to evaluate. The results were stated first by Hathaway (1988) without proof. A general proof in closed form is presented in Appendix D. The eigenfunctions describing $\mathcal{V}'_{\rm LS}$ are nearly orthogonal to $\mathcal{V}'_{\rm MF}$.[5] Once the coefficients L_m and S^0_ℓ are determined, the meridional flow may be reconstructed with (14) and the limb shift function may be reconstructed with

$$\mathcal{V}_{\rm LS}\left(B_0,\varrho\right) = \sum_{\ell=0}^{N_{LS}}\left[L_\ell\,\left(2\,\ell+1\right)^{-1/2}\,\mathcal{L}_\ell\left(1-\cos\varrho\right) + S^0_\ell\,\sqrt{\ell\,\left(\ell+1\right)}\,G_{{\rm MF},\ell}\left(B_0,\varrho\right)\right]. \tag{17}$$

Note that

$$\mathcal{V}_{\rm LS}\left(B_0,\varrho\right) + \mathcal{V}_{\rm MF}\left(B_0,\Phi,\Theta\right) = \mathcal{V}'_{\rm LS}\left(B_0,\varrho\right) + \mathcal{V}'_{\rm MF}\left(B_0,\Phi,\Theta\right). \tag{18}$$

---

[5]They are not exactly orthogonal because the observations on the disk are discrete and for simplicity we have orthogonalized these functions using continuous representations. See discussion in Section 3.4 and Figure 4.

3.2.4. Determination of the Bias

To determine the bias, each image is fit using the eigenfunctions described in Sections 3.2.1-3.2.3. Hathaway (1988, 1992, 1996) noted that strong magnetic fields can alter the convection pattern. He used an iterative procedure that first determines an estimate of the spectral coefficients and then replaces the Doppler estimates in pixels corresponding to strong magnetic fields with estimates consistent with these coefficients. The procedure repeats until there are no further significant changes in the spectral coefficients.

The present analysis diverges significantly from that previous work. The image at each stage of analysis is reformed into a column vectors $\boldsymbol{V}_{\text{LOS–1}}, \ldots, \boldsymbol{V}_{\text{LOS–3}}$ representing all of the N_{D} pixels located on the solar disk and $\boldsymbol{v}_{\text{LOS–1}}, \ldots, \boldsymbol{v}_{\text{LOS–3}}$ representing just the N_{W} weak field pixels corresponding to an absolute LOS magnetic field less than or equal to 10 G *or* minimal support (< 60) as determined by the disambiguation module ME_720s_fd10{disambig} of the vector pipeline.[6] For the 17 days under consideration N_{W} represents about 84% of the solar disk. In the same manner, two matrices of eigenfunctions are constructed $\mathbf{E}$ and $\mathbf{e}$ representing the $M = N_{\text{R}} + N_{\text{LS}} + N_{\text{MF}}$ eigenfunctions used to determine the large scale Doppler patterns where $\mathbf{E}$ represents all of the N_{D} pixels located on the solar disk and $\mathbf{e}$ represents just the N_{W} weak field pixels. The goal is to determine a set of spectral coefficients $\boldsymbol{b}$ from the N_{W} stage 1 Doppler estimates in column vector $\boldsymbol{v}_{\text{LOS–1}}$. Obviously with $N_{\text{W}} \simeq 10^7$ and $M \simeq 24$ there is no unique solution to the overdetermined

[6]Strong field pixels correspond to absolute LOS magnetic field greater than 10 G *or* significant support (≥ 60).

system

$$\mathbf{e}\boldsymbol{b} = \boldsymbol{v}_{\text{LOS–1}},$$

$$\begin{bmatrix} \mathsf{e}_{11} & \cdots & \mathsf{e}_{1M} \\ \vdots & \cdots & \vdots \\ \mathsf{e}_{N_{\text{W}}1} & \cdots & \mathsf{e}_{N_{\text{W}}M} \end{bmatrix} \begin{bmatrix} T_1^0 \\ \vdots \\ T_{N_R}^0 \\ L_0 \\ \vdots \\ L_{N_{\text{LS}}-1} \\ S_1^0 \\ \vdots \\ S_{N_{\text{MF}}}^0 \end{bmatrix} = \begin{bmatrix} v_{\text{LOS–1},1} \\ v_{\text{LOS–1},2} \\ v_{\text{LOS–1},3} \\ \vdots \\ v_{\text{LOS–1},N_{\text{W}}} \end{bmatrix}. \tag{19}$$

where $v_{\text{LOS–1},i}$ are the $i = 1, \ldots, N_{\text{W}}$ stage 1 weak field pixels determined from (A3b) because no general inverse of the eigenvectors $\mathbf{e}$ exists. Instead we attempt to find the solution which is best in a L_2 norm sense where $\boldsymbol{b}^*$ minimizes

$$\|\mathbf{e}\boldsymbol{b}^* - \boldsymbol{v}_{\text{LOS–1}}\|_2 \leq \|\mathbf{e}\boldsymbol{b} - \boldsymbol{v}_{\text{LOS–1}}\|_2 \tag{20}$$

among all possible spectral coefficients $\boldsymbol{b}$. This optimal solution is determined from directly the least-squares solution

$$\boldsymbol{b}^* = \left(\mathbf{e}^{\text{T}}\mathbf{e}\right)^{-1} \mathbf{e}^{\text{T}} \boldsymbol{v}_{\text{LOS–1}}, \tag{21}$$

where $\left(\mathbf{e}^{\text{T}}\mathbf{e}\right)^{-1} \mathbf{e}^{\text{T}}$ is known as the pseudo-inverse (Moore 1920; Bjerhammar 1951; Penrose 1955). Note that this approach explicitly ignores the strong field pixels in determining the spectral coefficients circumventing the iterations necessary in Hathaway (1996).

The temporally varying bias image for each full-disk Dopplergram of N_{D} pixels can then be reconstructed from

$$\boldsymbol{B} = \mathbf{E}\boldsymbol{b}^*. \tag{22}$$

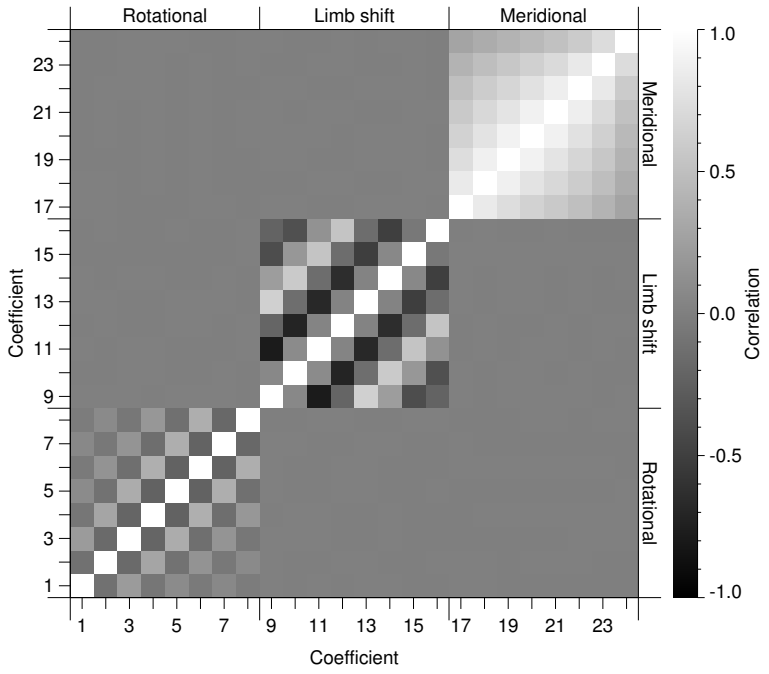

Fig. 4.— Correlations between the coefficients for the fit to the large scale flows on 2010-07-04 at 17:00:00.

The large-scale bias free stage 2 Dopplergrams are then determined from

$$\boldsymbol{V}_{\text{LOS–2}} = \boldsymbol{V}_{\text{LOS–1}} - \mathbf{E}\boldsymbol{b}^{*} \tag{23}$$

Figure 4 shows the correlations between the $M = 24$ coefficients used to fit the large scale Doppler patterns. The eigenfunctions are nearly block orthogonalized, *e.g.* there are correlations between the meridional eigenfunctions, but these eigenfunctions are completely decoupled from the limb-shift eigenfunctions validating the corrections encompassed by (16)-(18). Correlations within the block are expected as spherical harmonics themselves are not orthogonal on the observed solar hemisphere and they are further confused by their projection onto the LOS (Mochizuki 1992).

Figures 5-7 show rotational, limb shift, and meridional spectral coefficients during 17 days in 2010 as determined from (21). The black data are "high quality" data and the

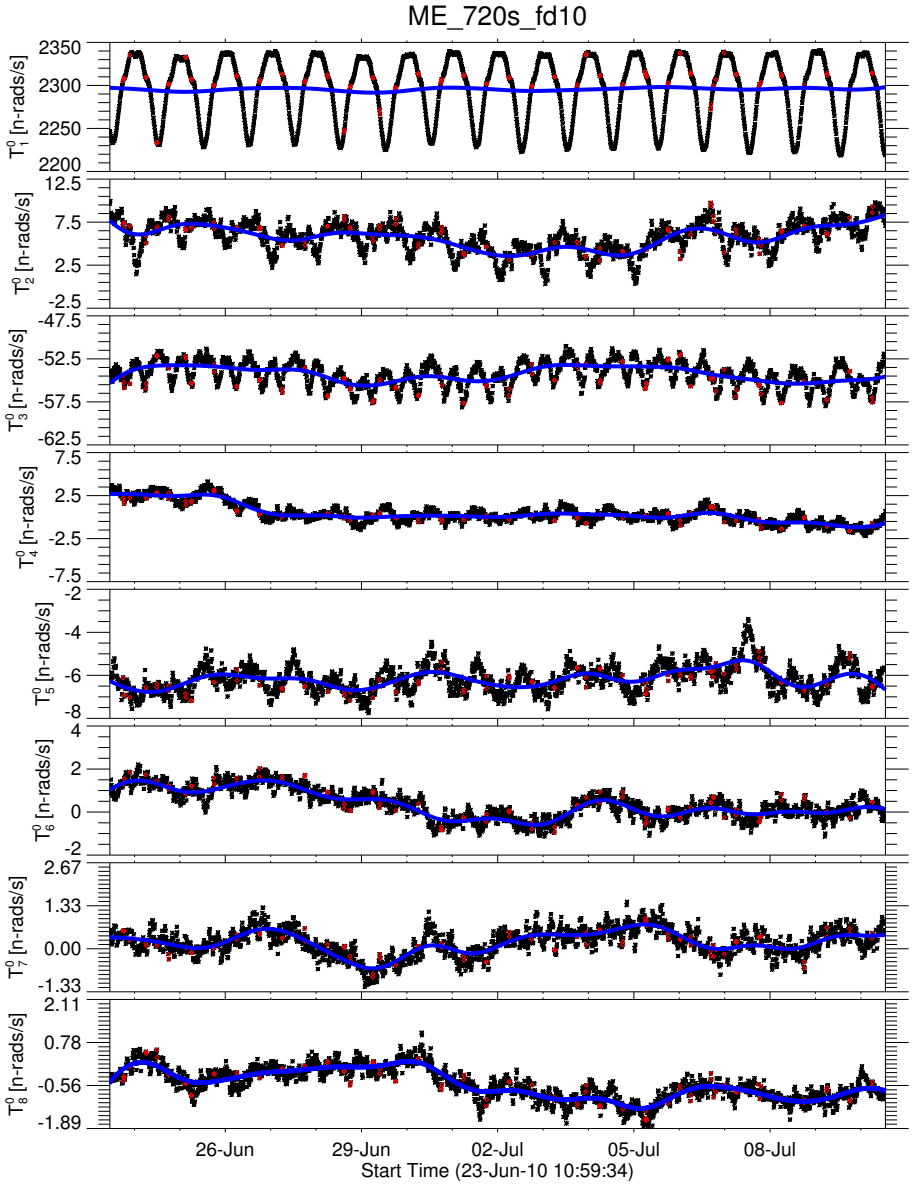

Fig. 5.— Rotational spectral coefficients during 17 days in 2010. The black data are "high quality" data and the red data are low quality data (Keyword: QUALITY $\neq 0$). The blue line corresponds to the low frequency trend determined after orbital artifacts are removed. See text for a complete discussion.

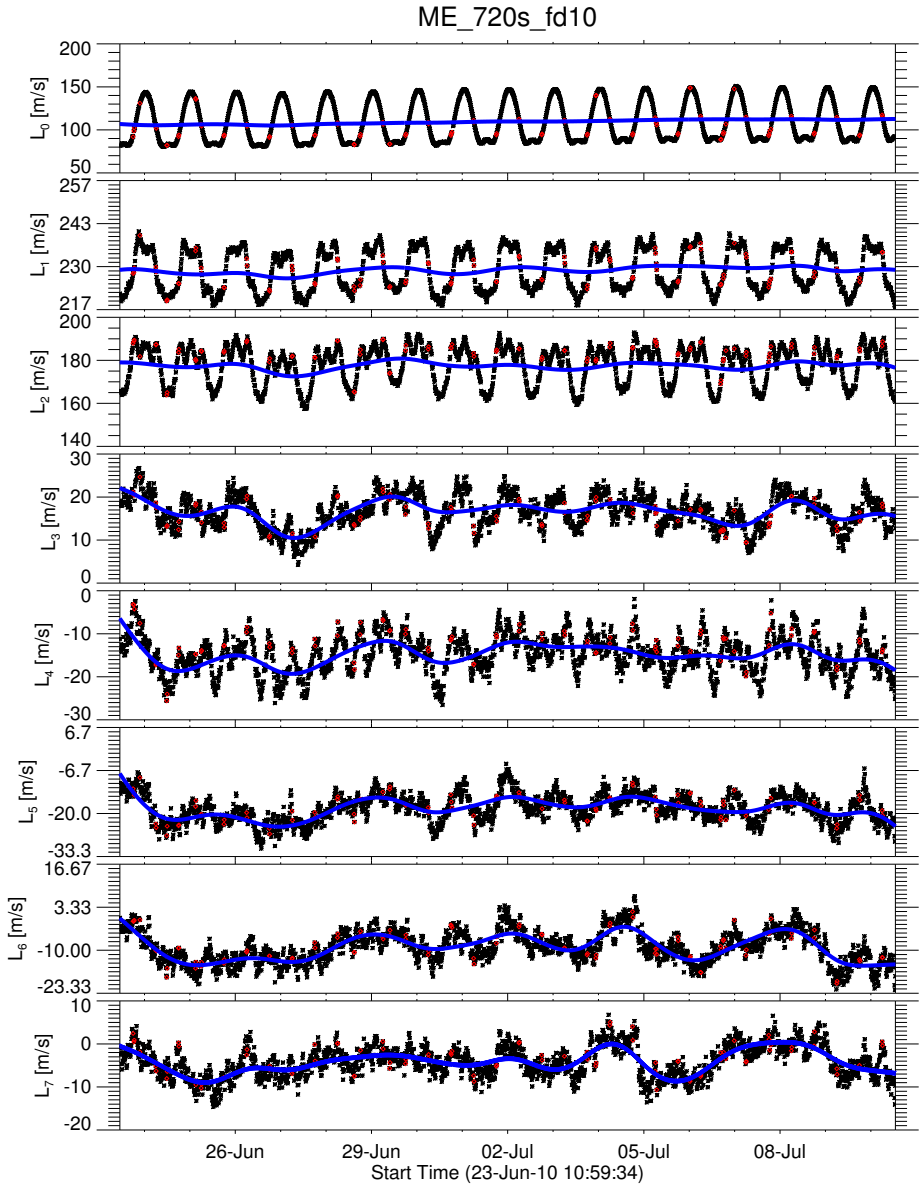

Fig. 6.— Limb shift spectral coefficients during 17 days in 2010. Same format at Figure 5.

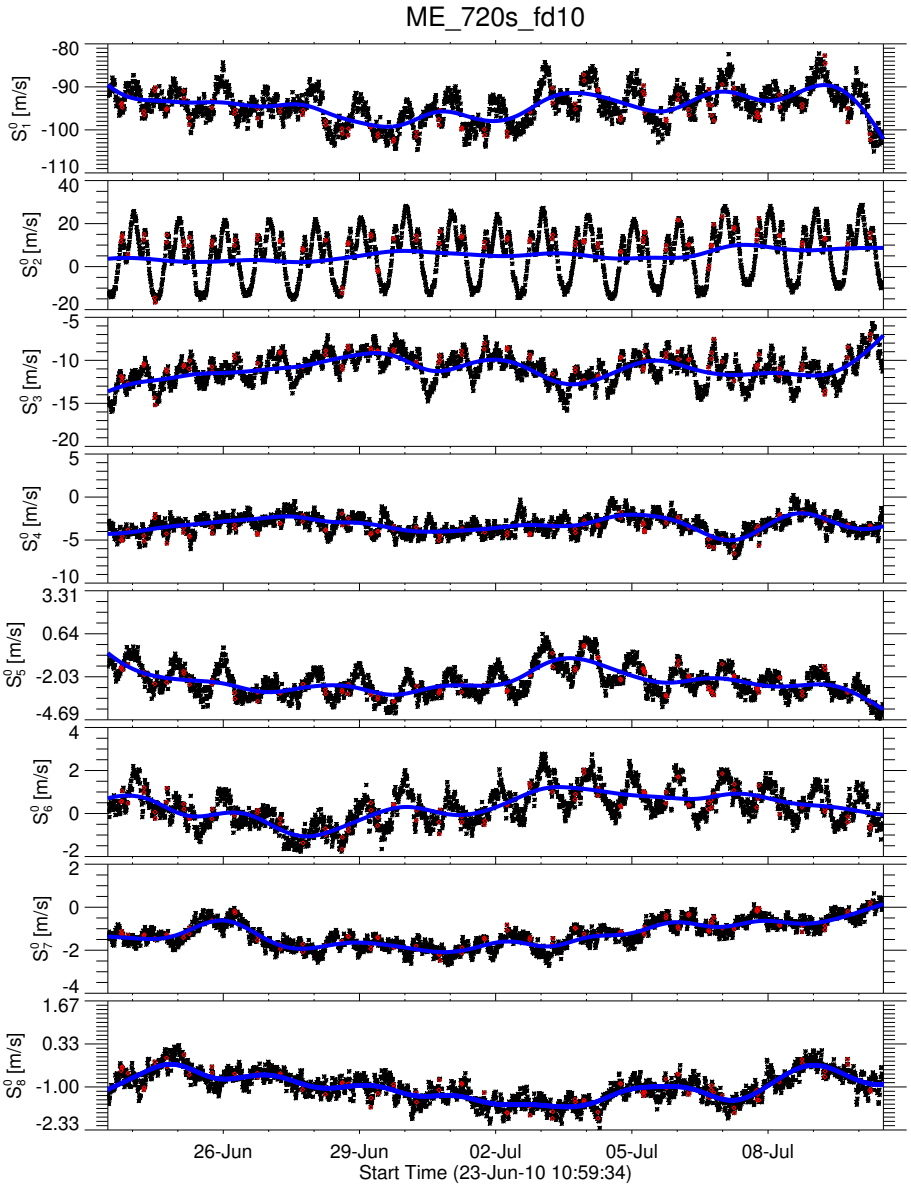

Fig. 7.— Meridional spectral coefficients during 17 days in 2010. Same format at Figure 5.

red data are "low quality" data (Keyword: QUALITY $\neq 0$). We emphasize that since the satellite velocity has been removed from each pixel prior to fitting the Doppler data there should be *no correlation* with the satellite velocity. However, clear aperiodic oscillations are present with a primary period of 24 hrs is observed in the lowest spectral coefficients in all three Figures. In Figure 5, the lowest coefficient exhibits a peak-to-peak amplitude 110 nrads/s or $\Delta v = \sqrt{2}\,\Delta T_1^0\,R_\odot \simeq 105$ m/s. Again, this indicates a significant error in the measurements particularly near the limb where solar rotation is the strongest in the LOS component. The blue line corresponds to the low-frequency trend with a cutoff period of 48 hrs determined from a nonparametric B-spline filter (Schuck 2010; Woltring 1986). The details of how this trend is determined is discussed in Section 3.4.

The red curve in Figure 3 shows the residual spatially averaged RMS Doppler velocity for the stage 2 Dopplergrams $\boldsymbol{V}_{\text{LOS–2}}$. Removing the time-vary bias considerably improves the temporal stability of the Dopplergrams. One of the most striking features of these data is the bias in the S_1^0 meridional coefficient exhibited by Figures 7. One explanation for this result is an average cross-equatorial flow of $\simeq -95$ m/s. A cross-equatorial flow of this magnitude would be easily detected by other techniques, so this explanation is ruled out. Another possible explanation for this bias is an error in position angle $\delta\psi = \tan^{-1}(S_1^0/A)$ in solar North where A is determined from (12a). A bias of $\simeq -95$ m/s corresponds to error in position angle of about 2.6°. This explanation also seems incorrect given the agreement between the alignment of HMI and MDI magnetogram data exhibited in Figure 1. Therefore, our conclusion at present is that this bias in the S_1^0 coefficient represents a spatial non-uniformity in the response of HMI.

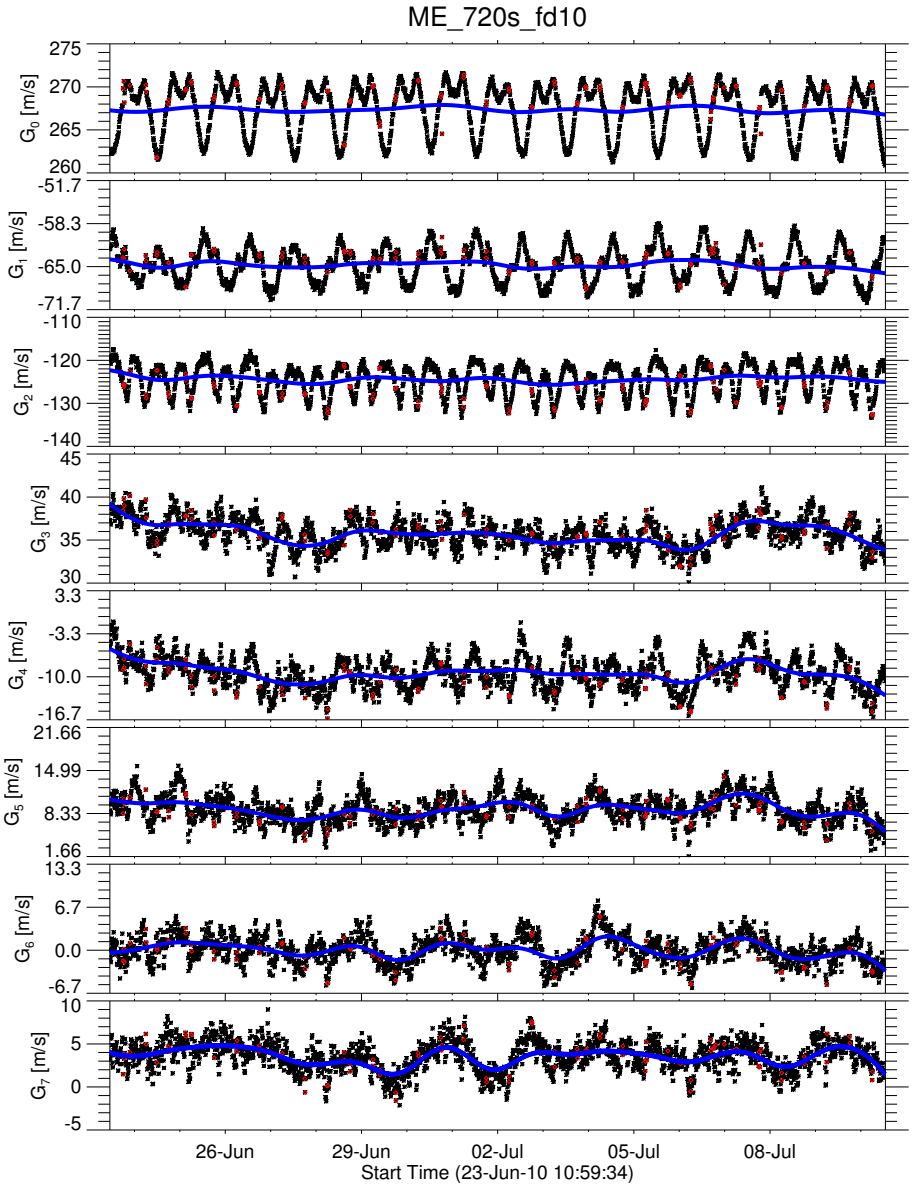

Fig. 8.— Gain coefficients during 17 days in 2010. Same format as in Figure 5.

3.3. Stage 3: Gain Adjustment

Figure 3 shows that even after the known velocities are removed from the HMI data, there still remains a strong daily periodicity in the residual images, indicating contamination by orbital effects. Therefore, stage 3 of our COADRED procedure consists of a pixel by pixel, image by image, adjustment of the gain. Given the strong aperiodic oscillations in the limb shift functions, we hypothesize that the gain of each pixel follows a similar pattern; consequently, we use the limb shift formalism to correct for this gain. Following the procedure in Section 3.2.4, two $\mathbb{R}^{N_{\rm D}\times N_{\rm G}}$ and $\mathbb{R}^{N_{\rm W}\times N_{\rm G}}$ matrices are constructed from the limb shift eigenfunctions, $\mathbf{E}_{\rm LS} = \mathbf{E}\left(1:N_{\rm D}, N_{\rm R}+1:N_{\rm R}+N_{\rm LS}+1\right)$ and $\mathbf{e}_{\rm LS} = \mathbf{e}\left(1:N_{\rm W}, N_{\rm R}+1:N_{\rm R}+N_{\rm LS}+1\right)$, corresponding to the $N_{\rm G} = N_{\rm LS}$ limb shift eigenfunctions used to fit the bias where $\mathbf{E}_{\rm LS}$ represents all of the $N_{\rm D}$ pixels located on the solar disk and $\mathbf{e}_{\rm LS}$ represents just the $N_{\rm W}$ weak field pixels. These eigenfunctions are then fit to the absolute value of the stage 2 bias subtracted Dopplergrams

$$\mathbf{e}_{\rm LS}\boldsymbol{g} = \left|\boldsymbol{v}_{\rm LOS\text{–}2}\right|,$$

$$\begin{bmatrix} \mathsf{e}_{10} & \cdots & \mathsf{e}_{1N_{\rm G}-1} \\ \vdots & \cdots & \vdots \\ \mathsf{e}_{N_{\rm W}0} & \cdots & \mathsf{e}_{N_{\rm W}N_{\rm G}-1} \end{bmatrix} \begin{bmatrix} G_0 \\ \vdots \\ G_{N_{\rm G}-1} \end{bmatrix} = \begin{bmatrix} \left|v_{\rm LOS\text{–}2,1}\right| \\ \left|v_{\rm LOS\text{–}2,2}\right| \\ \vdots \\ \left|v_{\rm LOS\text{–}2,N_{\rm W}}\right| \end{bmatrix}, \tag{24}$$

which has the optimal least-squares solution

$$\boldsymbol{g}^* = \left(\mathbf{e}_{\rm LS}^{\rm T}\mathbf{e}_{\rm LS}\right)^{-1}\mathbf{e}_{\rm LS}^{\rm T}\left|\boldsymbol{v}_{\rm LOS\text{–}2}\right|. \tag{25}$$

The gain for each image can then be reconstructed from

$$\boldsymbol{G} = \mathbf{E}_{\rm LS}\boldsymbol{g}^*. \tag{26}$$

Figure 8 shows the gain coefficients during 17 days in 2010 as determined from (25)

3.4. Treatment of the Coefficients and Image Reconstruction

Plotting the data in Figures 5-8 as a function of $V_{\rm R}$, reveals their systematic *nonlinear* dependence on radial satellite velocity as shown in Figures 9-12. The nonlinear response is the source of the aperiodic temporal dependence in the coefficients. The black data points in these figures are fit by weighted least squares with orthogonalized polynomials.[7] The weights for each data point are determined from the variance in the coefficients from the fits. The optimal polynomial order is determined using the Bayesian Information Criteria (Schwarz 1978; Ye et al. 2008)

$$\mathrm{BIC}_k \simeq N_{\rm D}\, \log \widehat{\sigma}^2_{\rm ML} + N_k\, \log N_{\rm D}, \tag{27}$$

where $N_{\rm D}$ is the number of data, N_k is the number of model parameters and $\widehat{\sigma}^2_{\rm ML}$ is the maximum likelihood estimate of the variance. The optimal number of coefficients $k_{\rm opt}$ corresponds to the model with the minimum BIC_k value.[8] We emphasize that the "model" involves two separate fitting processes: (1) The orthogonalized polynomial fit to the parameterized data in V_R space and (2) the temporal fit using a nonparametric B-spline filter to remove any systematic temporal drift in the parameters which would bias the orthogonalized polynomial fit. The B-spline filter has some attractive properties for this problem as data frames are missing and a B-spline filter can be interpreted as an optimal cascaded Butterworth filter generalized for unevenly sampled data (Craven & Wahba 1979). The number of degrees of freedom removed from the data by the smoothing procedure can be determined from the trace of the influence matrix of the B-spline filter (Wahba 1980; Woltring 1986). The maximum likelihood estimate of the error variance is computed from

[7]The red "low quality" data are ignored.

[8]The application of BIC does not require that the true model is in the set of models (polynomials) under consideration (Cavanaugh 1999).

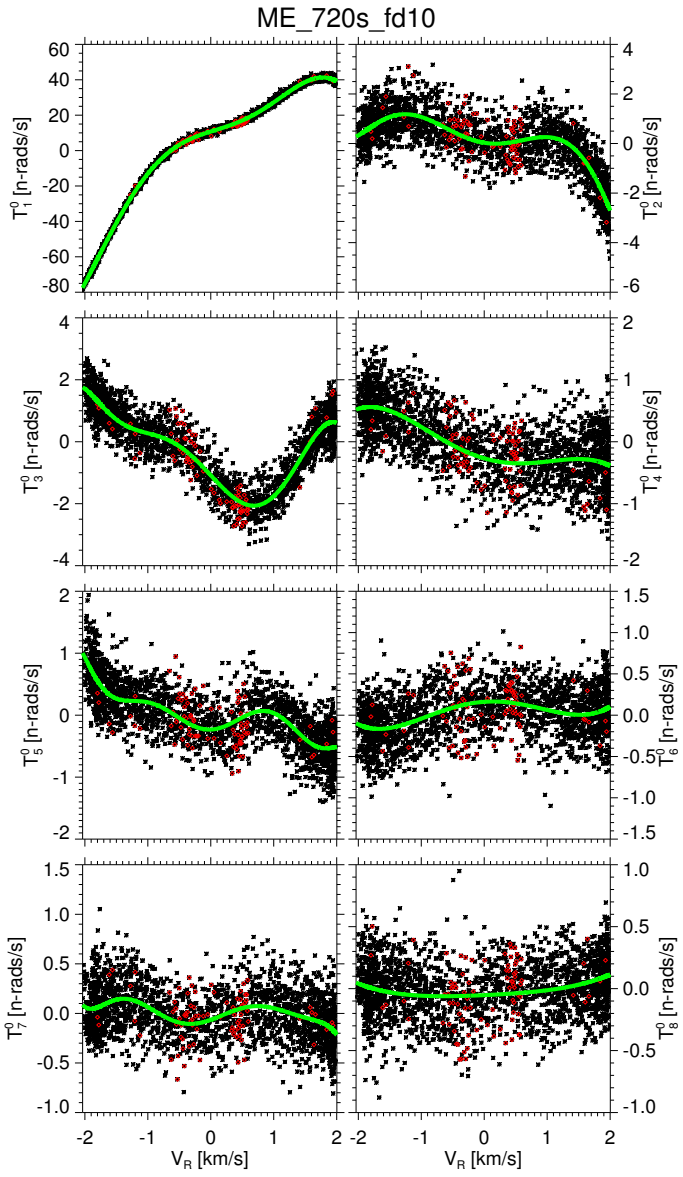

Fig. 9.— Rotational spectral coefficients during 17 days in 2010 as a function of satellite radial velocity $V_{\rm R}$. The black data are "high quality" data and the red data are low quality data (Keyword: QUALITY $\neq 0$). The green line corresponds to the "best" fit of orthogonalized polynomials as determined by the BIC.

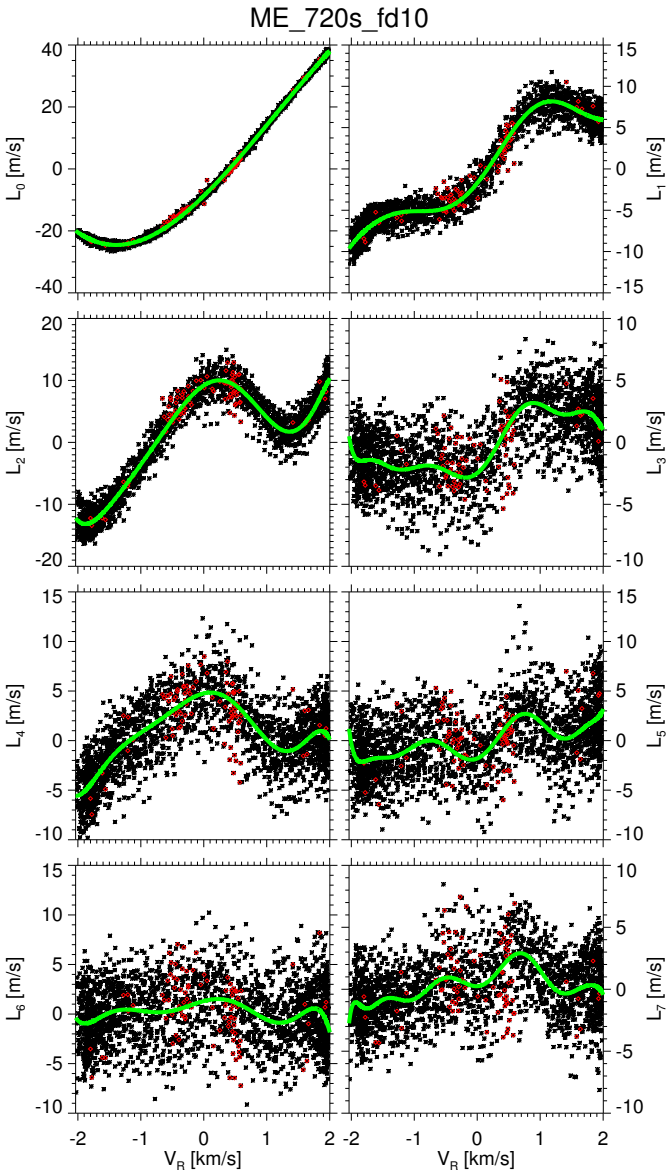

Fig. 10.— Limb shift spectral coefficients during 17 days in 2010 as a function of satellite radial velocity $V_{\rm R}$. Same format at Figure 9.

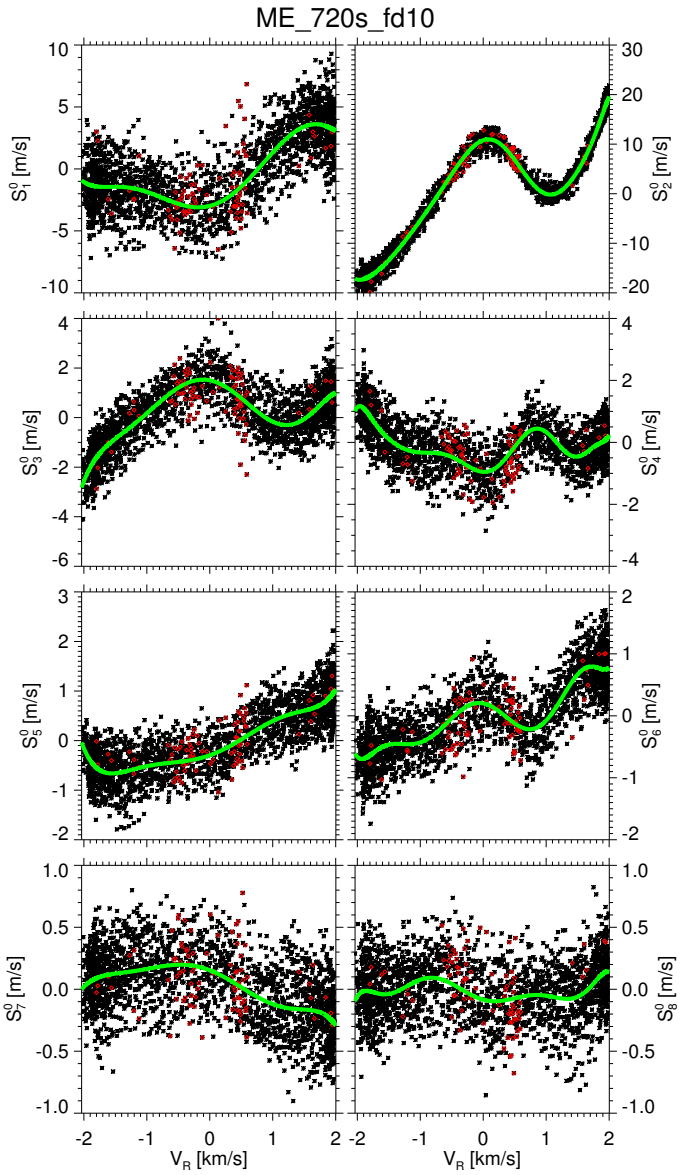

Fig. 11.— Meridional spectral coefficients during 17 days in 2010 as a function of satellite radial velocity $V_{\rm R}$. Same format at Figure 9.

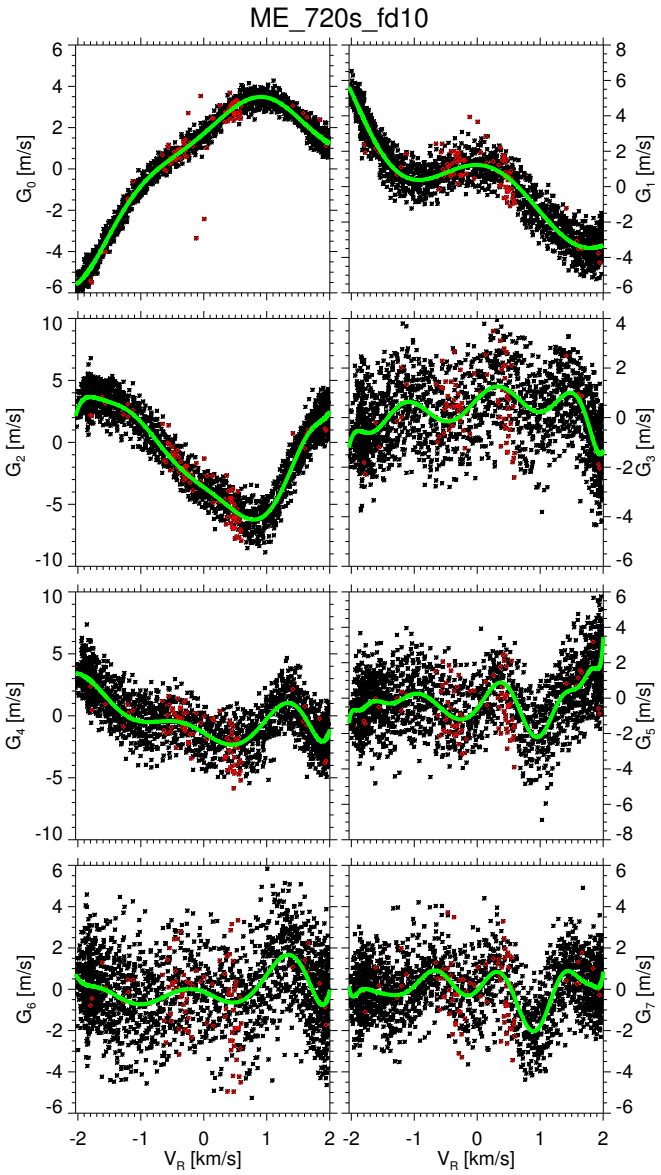

Fig. 12.— Gain coefficients during 17 days in 2010 as a function of satellite radial velocity $V_{\rm R}$. Same format at Figure 9.

the residuals by subtracting both of these fits from the stage 1 data and therefore N_k in (27) must reflect both of these fitting processes, *i.e.* the order of the orthogonalized polynomial and the trace of the influence matrix of the B-spline filter. The smoothing parameter of the B-spline filter is fixed with a cutoff of 48 hrs and some iteration is necessary to minimize the BIC and find the optimal coefficients for each polynomial order k.

Using the low frequency response and the orthogonalized polynomial fit corresponding to the blue and green curves in Figures 5-8, a model for the *predicted* bias and gain coefficients may be determined for any radial velocity $V_{\rm R}$ time t in the data set

$$\boldsymbol{\beta}\left(V_{\rm R},t\right)=\boldsymbol{\beta}_{\rm LF}\left(t\right)+\boldsymbol{\beta}_{\rm OP}\left(V_{\rm R}\right), \tag{28a}$$

$$\boldsymbol{\gamma}\left(V_{\rm R},t\right)=\underbrace{\boldsymbol{\gamma}_{\rm LF}\left(t\right)}_{\rm blue}+\underbrace{\boldsymbol{\gamma}_{\rm OP}\left(V_{\rm R}\right)}_{\rm green}. \tag{28b}$$

The stage 3 Dopplergrams are reconstructed by subtracting off the *observed* bias and dividing by the *observed* gain, then multiplying by the *predicted* gain and adding back the *predicted* bias at a consistent radial velocity $V_{\rm R}\equiv 0$

$$\boldsymbol{V}_{\rm LOS\text{–}3}=\left[\mathbf{E}_{\rm LS}\boldsymbol{\gamma}\left(0,t\right)\right]\oslash\left[\mathbf{E}_{\rm LS}\boldsymbol{g}^{*}\right]\odot\left[\boldsymbol{V}_{\rm LOS\text{–}1}-\mathbf{E}\boldsymbol{b}^{*}\right]+\mathbf{E}\boldsymbol{\beta}\left(0,t\right), \tag{28c}$$

where $\oslash$ and $\odot$ represent Hadamard (element-wise) division and multiplication of vectors.

These stage 3 Dopplergrams are the final result of our COADRED procedure. It is important to note that (28c) does not *correct* the images in some absolute sense; however, it does remove the *inconsistencies* caused by the orbital artifacts. The blue curve in Figure 3 shows the residual spatially averaged RMS Doppler velocity for the stage 3 Dopplergrams $\boldsymbol{V}_{\rm LOS\text{–}2}$. Removing the time-vary bias and spatially and temporally adjusting the gain greatly improves the temporal stability of the Dopplergrams. The difference in variability between the black curve (stage 1) and blue curve (stage 3) is roughly 31dB.

The reduction in RMS velocity shown in Figure 3 is striking. This result indicates that the COADRED procedure is highly effective at removing orbital effects, at least, on large

scales. The key questions, however, are whether it is robust in that it removes artifacts from all scales and whether it is accurate in that the procedure introduces no new artifacts to the data. In order to answer these question, we perform below a detailed spectral analysis of the images after each COADRED stage. This analysis shows that the procedure does clean the data from orbital artifacts at all spatial scales and that it does not contaminate the data with new artifacts.

4. Analysis of Stages-1–3

SDO produces an overwhelming amount of data. Even for the reduced data series considered here, there are 20×10^9 pixels to analyze over the 17 day period. Further complicating the analysis, data frames are lost in any long data series from *SDO*, and consequently the sample rates are nonuniform. These data require techniques that scale well with $N_{\rm D} \simeq 10^7$, the number of pixels in each image and $N_t \simeq 10^3$, the number of images and methods that are either insensitive to the sample rates or that are explicitly designed to analyze non-uniformly sampled data. For this data set we implement the Karhunen-Loéve (KL) transform (Loéve 1955; Lumley 1967; Sirovich 1987; Holmes et al. 1996) briefly described in Appendix D.1 combined with the CLEAN algorithm for computing power spectral density of unevenly sampled time-series (Roberts et al. 1987; Högbom 1974). The KL transform decomposes the dynamics into a set of $N_{\rm D} \times N_t$ orthogonal spatial modes $\mathbf{\Phi}$ and $N_t \times N_t$ temporal coefficients $\boldsymbol{\alpha}$ with $N_t \ll N_{\rm D}$. The advantage of this analysis is that the temporal dynamics of the entire image sequence is represented by a relatively small matrix $\boldsymbol{\alpha}$ in contrast to attempting to interpret to spectral properties of $N_{\rm D} \times N_t$ pixels in the image sequence. The disadvantages of the technique are that the spatial information associated with the dynamics is decoupled from the temporal dynamics and the spatial modes are purely empirical – there isn't always an simple physical interpretation for the

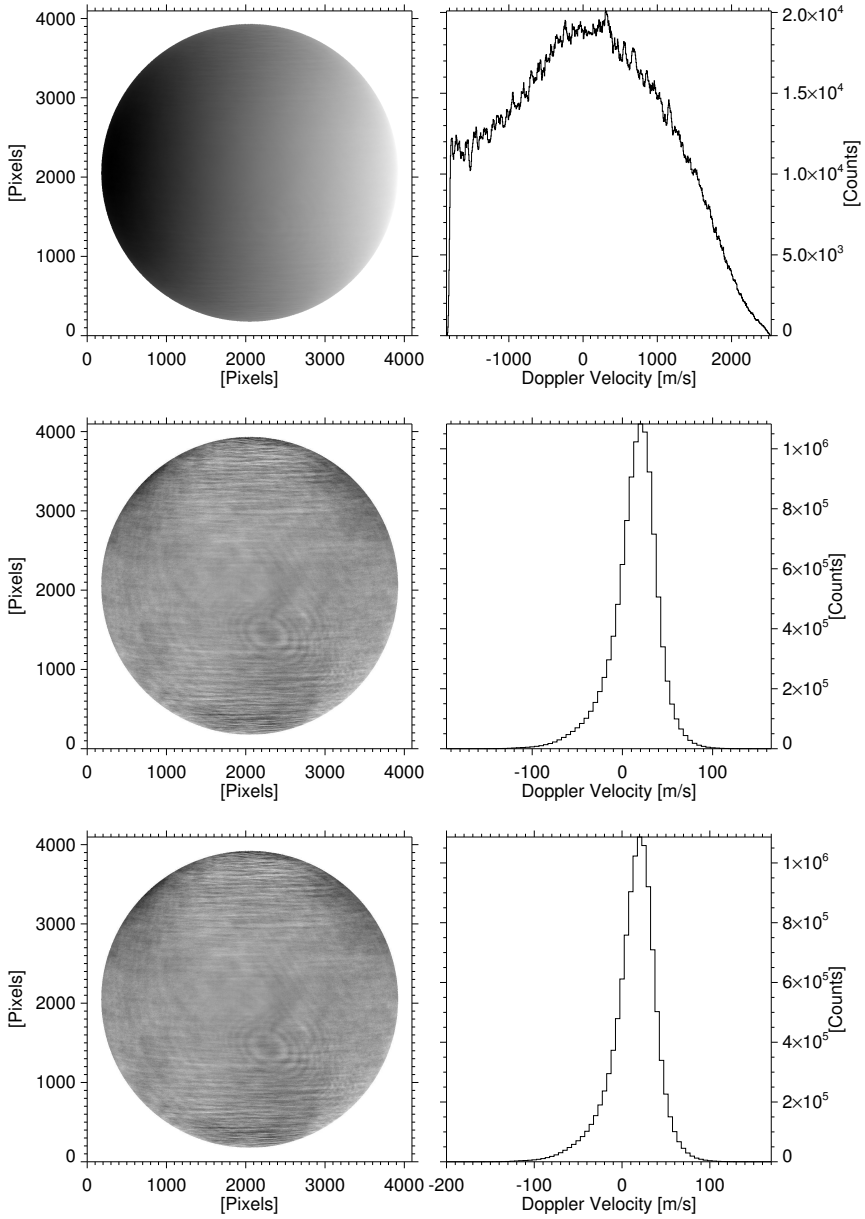

Fig. 13.— Median Co-aligned Doppler image and histogram after various stages of processing: The top is stage 1, the middle is stage 2, and the bottom is stage 3. The stage 1 image is dominated by the time-averaged differential rotation, limb shift and meridional flow patterns. The middle and bottom panels exhibit a clear Fresnel pattern.

spatial structure of the modes. Using the CLEAN algorithm on the coefficient matrix $\boldsymbol{\alpha}$ completely characterizes the spectral properties of the data as the spatial eigenfunctions $\boldsymbol{\Phi}$ are orthogonal.

The images for the various stages are first co-aligned and registered into a data cube or image sequence denoted $\boldsymbol{I}'$ which is $\mathbb{R}^{N_{\rm D}\times N_t}$. The median is determined for each stage via

$$\langle \boldsymbol{I} \rangle_i = \text{median}_j \left(\boldsymbol{I}'_{ij} \right) , \tag{29a}$$

where $\langle \boldsymbol{I} \rangle_i$ is understood to be the temporal median of each pixel in N_t images. This median is then subtracted from each image

$$\boldsymbol{I}_{ij} = \boldsymbol{I}'_{ij} - \langle \boldsymbol{I} \rangle_i . \tag{29b}$$

Figure 13 shows the median co-aligned Doppler image and histogram after various stages of processing: The top is stage 1, the middle is stage 2, and the bottom is stage 3. The stage 1 image is dominated by the time-averaged differential rotation, limb shift and meridional flow patterns. The middle and bottom panels exhibit a clear Fresnel pattern.

The KL transform is used to decompose this image sequence into a $\mathbb{R}^{N_t\times N_t}$ matrix of orthogonal coefficients $\boldsymbol{\alpha}$ and an $\mathbb{R}^{N_{\rm D}\times N_t}$ matrix of orthogonal spatial modes $\boldsymbol{\Phi}$. In general, the KL modes have the following temporal and spatial properties $\Delta T \simeq 1/\#$ and $\Delta L \simeq 1/\#$, *i.e.*, higher mode numbers (#'s) correspond to faster time-scales and smaller spatial-scales. Figure 14 shows the eigenvalue spectra after the various stages of analysis: 1 (black), 2 (red), and 3 (blue). While stages 2 and 3 are very similar, stage 1 which contains both orbital effects in the large scale bias and the small scale velocities is significantly different for the three lowest modes and perhaps as high as mode #5. This eigenvalue spectra can be interpreted as "variance explained" by each of the modes. Figures 15-17 show the spatial eigenfunctions and temporal behavior of the coefficients of modes #1 and #2 for stages 1, 2, and 3. Note the oddly shaped distribution of spatial power and

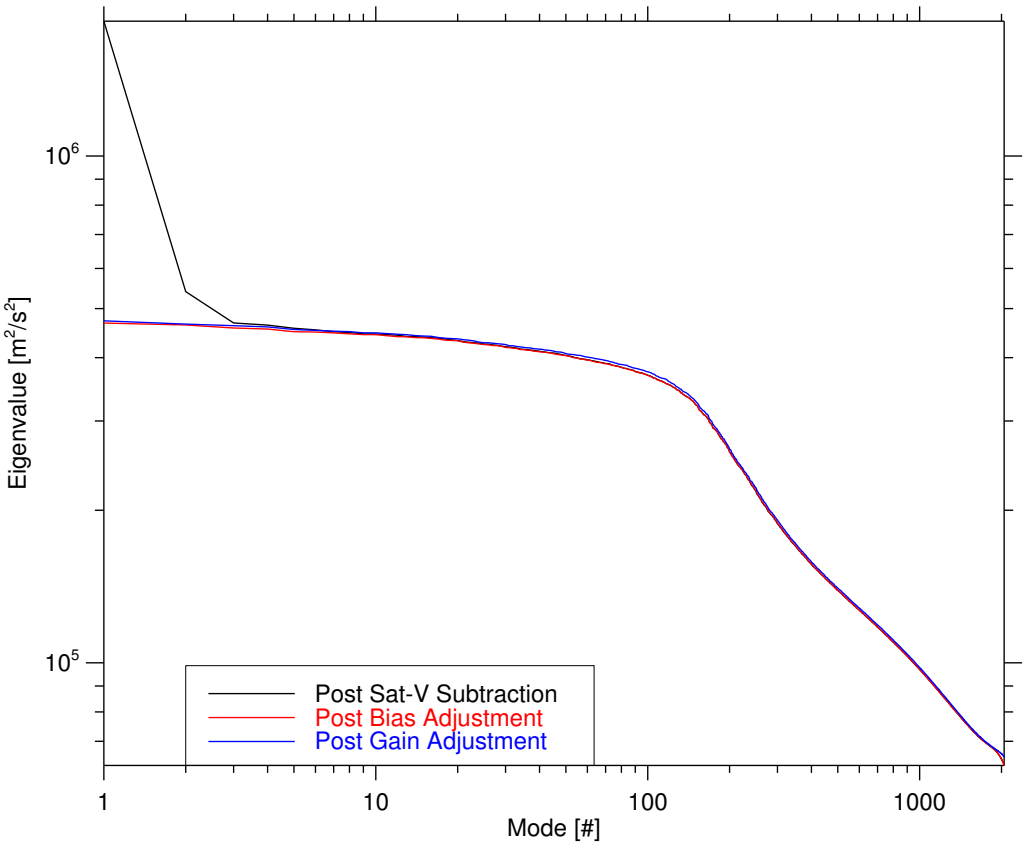

Fig. 14.— KL eigenvalue spectra after the various stages of analysis: 1 (black), 2 (red) and 3 (blue).

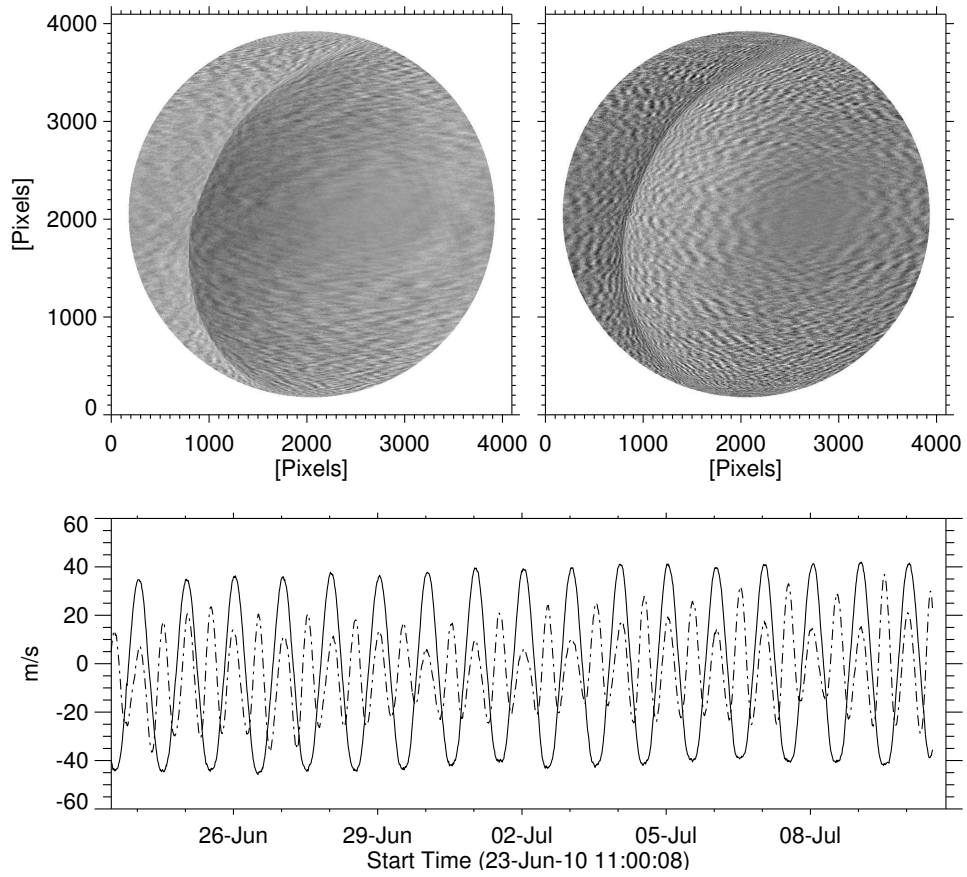

Fig. 15.— Top: spatial KL modes #1 and #2 for stage 1. Bottom: time history of the coefficients for modes #1 (solid) and #2 (dashed). Note the oddly shaped distribution of spatial power and the nearly periodic behavior of the coefficients.

the nearly periodic behavior of the coefficients cause by the time-varying bias and gain in Figure 15 for stage 1.

Figure 18 shows the power in the coefficients of the KL transforms ($\boldsymbol{\alpha}^2$) as a function of time for the stage 1 (left column), stage 2 (middle column), and stage 3 (right column) data. The top/middle/bottom panels correspond to a magnified view of modes 1500-2045, 1-200, and 1-10 lowest modes for each stage. The stage 1 data (left column) exhibits a clear daily periodicities as expected from Figure 15 and an overall daily modulation of the power

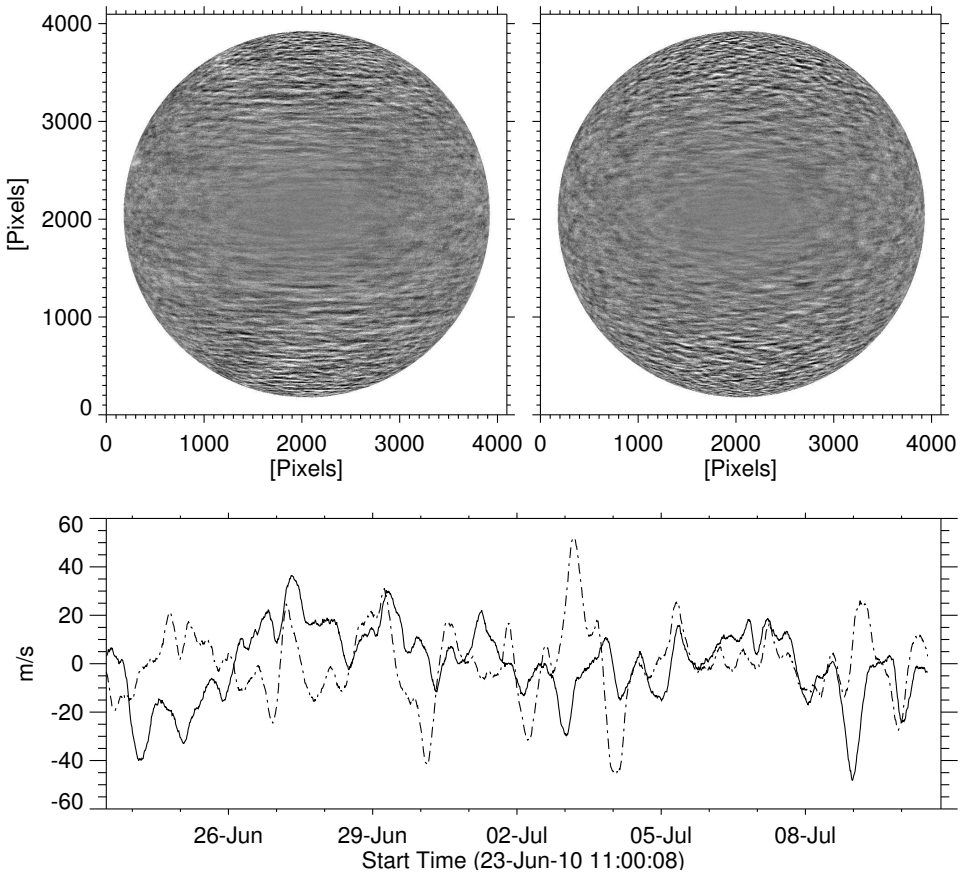

Fig. 16.— Top: spatial KL modes #1 and #2 for stage 2. Bottom: time history of the coefficients for modes #1 (solid) and #2 (dashed).

particularly evident below mode 50 in the middle panel and above mode 1700 in the top panel. The stage 2 data (middle column), after the large scale flows have been removed, is improved at the lowest few modes in the bottom panel reinforcing the concept that the lowest KL modes correspond to the slowest time-scales and the largest spatial scales. The stage 3 data (right column), after gain adjustment, is dramatically more uniform than the stage 1 and stage 2 data in the top and middle panels. Despite the improvement, there remain some temporal artifacts in the power of the highest mode numbers for the stage 3 data.

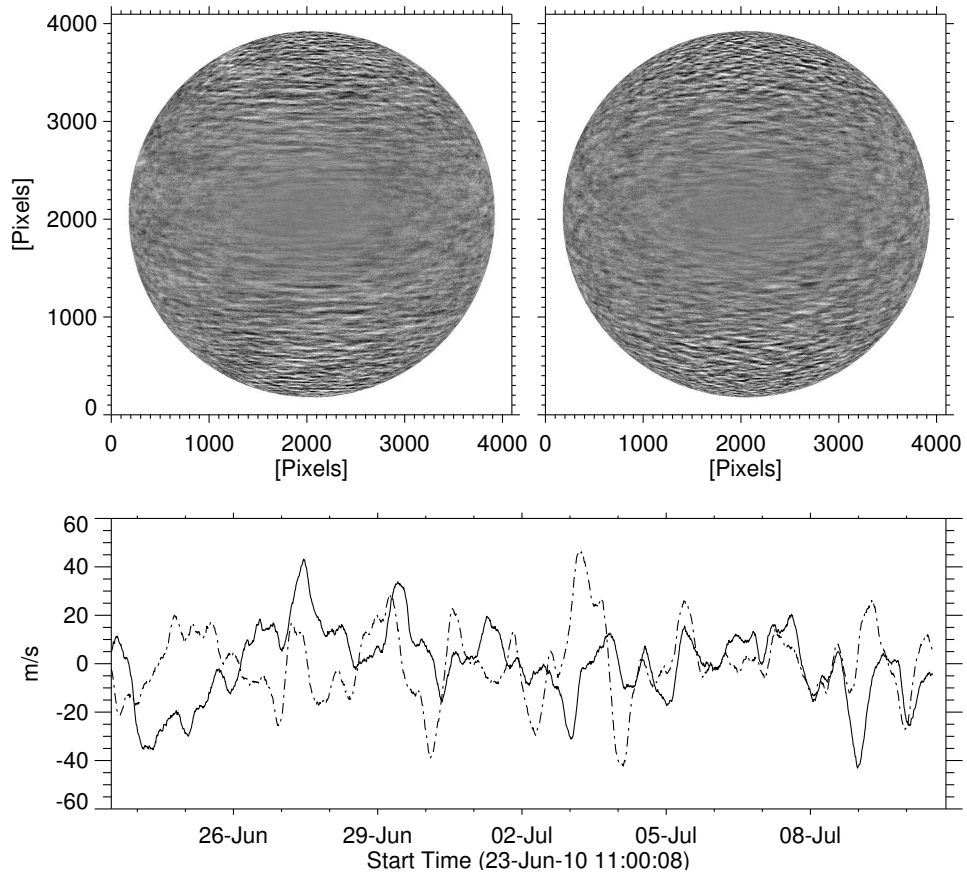

Fig. 17.— Top: spatial KL modes #1 and #2 for stage 3. Bottom: time history of the coefficients for modes #1 (solid) and #2 (dashed).

The CLEAN algorithm (Roberts et al. 1987; Högbom 1974) is used to estimate the power spectral density of the KL-modes for each stage. The CLEAN algorithm performs a nonlinear devolution of the unevenly temporally sampled coefficients $\boldsymbol{\alpha}$ in the frequency domain to attempt to minimize the spectral artifacts introduced by the sampling function. Figure 19 shows the power spectral density in the coefficients of the KL transforms ($\boldsymbol{\alpha}^2$) for stage 1 (left column), stage 2 (middle column), and stage 3 (right column) data estimated using the CLEAN algorithm with a gain of 0.05 and about 1400 iterations. . The middle row is a magnified view of the 10 lowest modes from 0-5 cycles/day for each stage corresponding to the small box in the lower left hand corner of the panels in the top row. The bottom

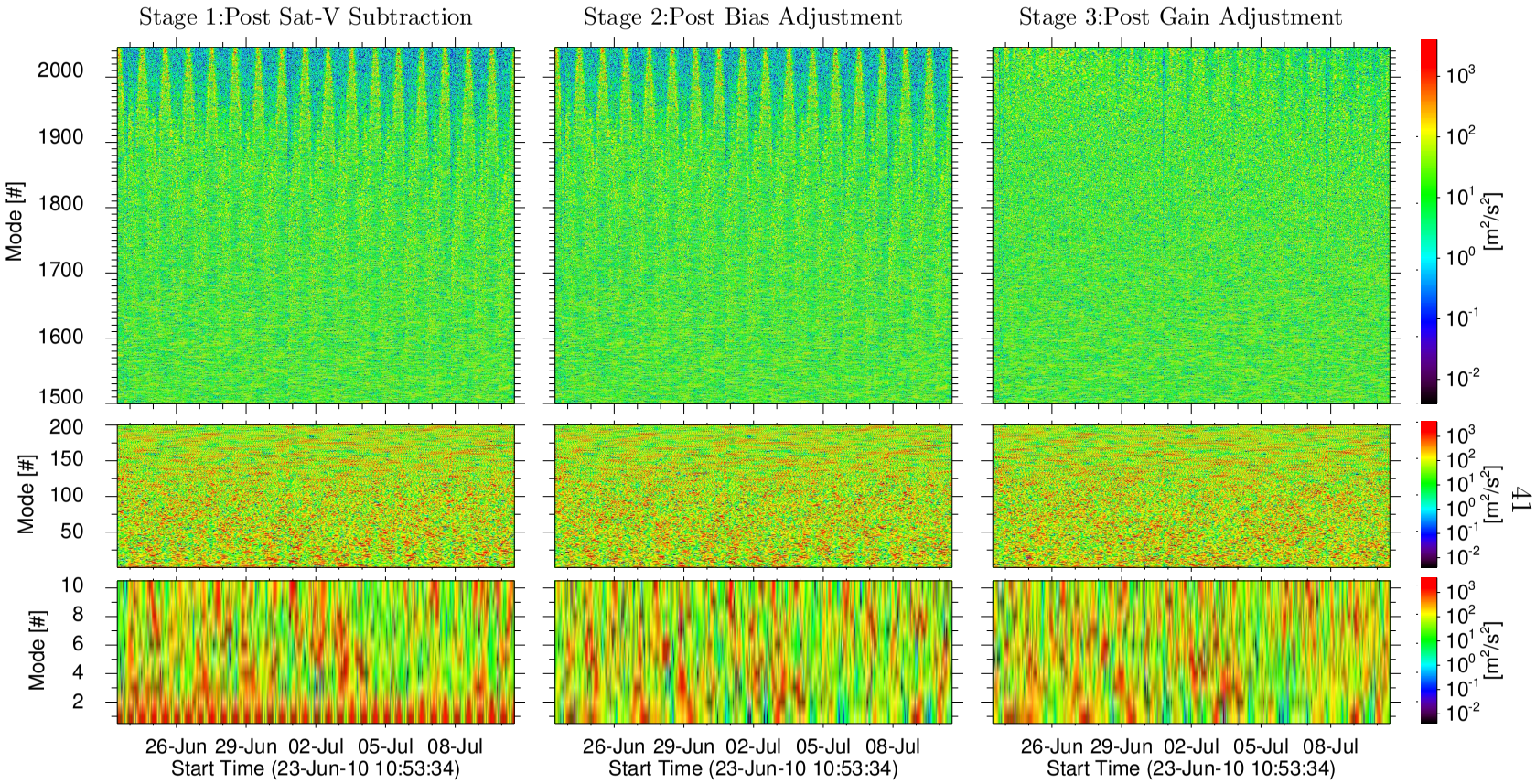

Fig. 18.— Power in the coefficients of the KL transforms ($\boldsymbol{\alpha}^2$) for stage 1 (left column), stage 2 (middle column), and stage 3 (right column) data. The top/middle/bottom panels correspond to a magnified view of modes 1500-2045, 1-200, and 1-10 for each stage.

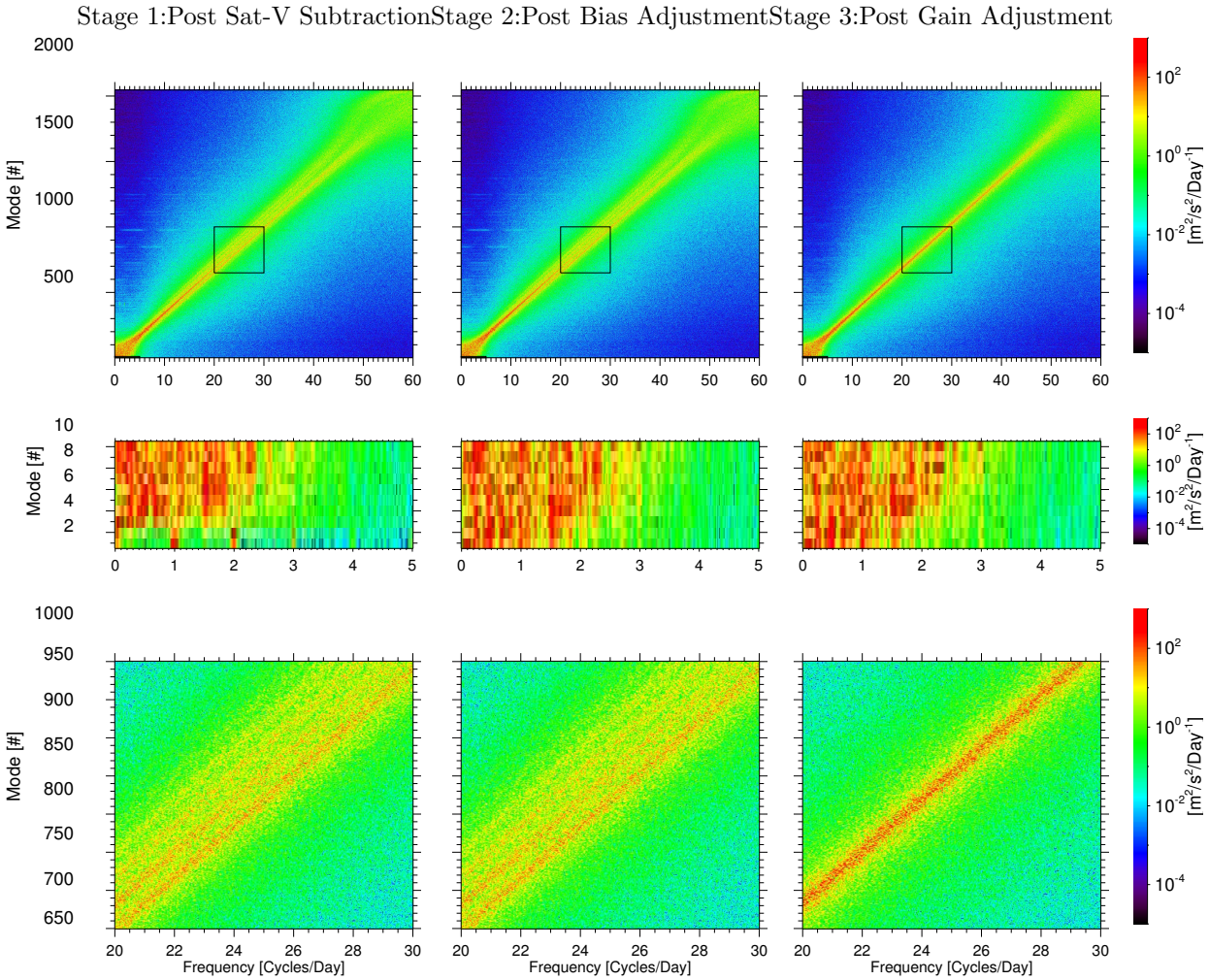

Fig. 19.— Power spectral density in the coefficients of the KL transforms ($\boldsymbol{\alpha}^2$) for stage 1 (left column), stage 2 (middle column), and stage 3 (right column) data estimated using the CLEAN algorithm with a gain of 0.05 and about 1400 iterations. The middle row corresponds to a magnified view of the 10 lowest modes from 0-5 cycles/day for each stage corresponding to the small box in the lower left hand corner of the panels in the top row. The bottom row is a magnified view of the modes 650-1000 from 20-30 cycles/day for each stage corresponding to the box in the lower near the middle of each panel in the top row.

row corresponds to a magnified view of the modes 650-1000 from 20-30 cycles/day for each stage corresponding to the box in the lower near the middle of each panel in the top row.

The general features of the top panel are a low frequency 0-5 cycles/day signature from modes 0-100 with a narrow dispersion relationship $f \simeq \#$ above that. The low frequency signature is produced by large scale features moving across the solar disk where as the narrow dispersion relation is caused by small scale convective features moving across the disk. This narrow dispersion relationship exhibits harmonics above mode 200. The spectral signatures of the orbital artifacts in the large scale flows is exhibited in the middle panel of the first column. Significant isolated spectral peaks are present at 1 and 2 cycles/day in mode 1 and at 1, 2, and 3 cycles/day in mode 2. There are also harmonics at 1, 2, and 3 cycles/day near mode 400 in the top left panel. These spectral signatures are largely mitigated after the removal of the large scale flow bias as shown by the panels in the middle and right columns. However, what remains in the middle column is multiple harmonics of the narrow dispersion relationship $f \simeq \#$. These harmonics are cause by the modulation in the amplitude of convective structures as they rotate across the disk. The stage 3 data shows that the spatially and temporally dependent gain adjustment included in (24) considerably reduces the affect of this modulation by collapsing the harmonics to a single peak at $f \simeq \#$.

5. Discussion and Conclusions

It is important to note that the stage 3 data cannot be claimed to be *more accurate*, only that it is *more consistent* from Dopplergram-to-Dopplergram. There are still artifacts which remain in the data shown in the right column of Figures 18 and 19, however, this is clearly a dramatic improvement in the quality of the Doppler data. While it is well known that the Milne-Eddington inversion of the HMI Pipeline data contains orbital artifacts

up to harmonics of several cycles/day (Hoeksema et al. 2014), the important take-away from the left hand column of Figures 18 and 19 is that *all temporal and spatial scales are contaminated by the orbital artifacts!* We know of no simple post-processing that will filter each spatial scale appropriately to remove the harmonics. It would be very surprising if the same conclusion did not also apply to the other critical observables produced by the Milne-Eddington inversion of the HMI Pipeline data such as the magnetic field data. Furthermore, if similar contamination is present in the 45 second Dopplergrams observed by Camera#2, we speculate that the modulation of the observations will affect the amplitude of the 5 minute oscillations critical to Helioseismic observations.

The important new result of this paper is that the COADRED procedure does successfully remove the orbital artifacts in the HMI Doppler data. Figure 3 shows that the improvement in the data is dramatic; the daily oscillations are almost completely eliminated. Furthermore, the procedure is robust in that as shown by Figure 19, it cleans the data on all spatial scales without introducing new artifacts. The COADRED procedure is straightforward to implement and will work on any data set of HMI Dopplergrams, consequently, we recommend that our procedure, or some modification, be incorporated into any HMI data analysis investigation. A key feature of the procedure is the use of the limb shift eigenfunctions to correct the gain in each pixel. The fact this gain correction is so successful has major implications for the possible mechanisms giving rise to the HMI errors and, consequently, for removing these errors from the vector magnetograms, as well. If we can correct the vector magnetograms to same level of fidelity as that shown by Figures 3 and 19, the resulting data would be invaluable for studying solar coronal structure and dynamics.

Peter Schuck acknowledges the support of the NASA LWS and GI programs and NASA/GSFC bridge funding in completing this work. He also gratefully acknowledges

useful conversations with Peter Williams, Mark Linton, Jesper Schou, David Hathaway, Yang Liu, Todd Hoeksema, and Phil Scherrer. K.D. Leka, Graham Barnes, and Peter Schuck were supported by NASA GI contracts NNH12CG10C: "Photospheric Properties of Flaring vs. Flare-Quiet Active Regions: Can we use HMI Vector Magnetogram Sequences to Quantify 'When and Why does the Sun go Boom?'" and NNH12CC03C: "Using SDO/HMI Data to Investigate the Energization of the Coronal Magnetic Field." We also gratefully acknowledge the help of Steve Martin who configured "houdini" our 80 core, 2TB shared memory system which was indispensable in the calculations. We also acknowledge the use of GNU Parallel (Tange 2011).

A. Observer Motion

Using Heliocentric-Cartesian coordinates (x, y, z), the z-axis is defined along the axis parallel to the observer-Sun line, pointing towards the observer. The y-axis is define to be perpendicular to that line and in the plane with the z-axis and the solar North pole with y increasing towards solar North. The x-axis is defined to be perpendicular to both the y- and z-axes with x increasing towards solar West. The location of a feature on the disk is given by (see eq. (17) in Thompson 2006)

$$x = -\, d\, \sin\theta_\rho\, \sin\psi, \tag{A1a}$$

$$y = d\, \sin\theta_\rho\, \cos\psi, \tag{A1b}$$

$$z = D_\odot - d\, \cos\theta_\rho, \tag{A1c}$$

where θ_ρ is the helioprojective angle, ψ is the position angle defined counter-clockwise from solar North, d is the distance between the feature and the observer, and $D_\odot$ is the distance between the observer and Sun center. The LOS vector pointing *from* the feature *to* the

observer is then

$$\widehat{\boldsymbol{\eta}}_{\mathbf{LOS}}\left(\theta_\rho,\psi\right)=\sin\theta_\rho\,\sin\psi\,\widehat{\boldsymbol{x}}-\sin\theta_\rho\,\cos\psi\,\widehat{\boldsymbol{y}}+\cos\theta_\rho\,\widehat{\boldsymbol{z}}. \tag{A2}$$

This implies that the raw observed Doppler velocity at each pixel (stage 0) can be expressed as

$$v_{\text{LOS–0}}=\widehat{\boldsymbol{\eta}}_{\mathbf{LOS}}\cdot\boldsymbol{V}_{SDO}-\widehat{\boldsymbol{\eta}}_{\mathbf{LOS}}\cdot\boldsymbol{U}_{\text{surface}}, \tag{A3a}$$

and the data with the satellite velocity subtracted or the "V-sat subtracted" (stage 1) data may be expressed as

$$v_{\text{LOS–1}}=v_{\text{LOS–0}}-\widehat{\boldsymbol{\eta}}_{\mathbf{LOS}}\cdot\boldsymbol{V}_{SDO}\equiv-\widehat{\boldsymbol{\eta}}_{\mathbf{LOS}}\cdot\boldsymbol{U}_{\text{surface}}. \tag{A3b}$$

B. Stonyhurst Unit Vectors

Since we are describing the sun in Stonyhurst coordinates, the unit vectors must be determined to resolve the projection of various vector quantities onto the LOS. The transformation between Stonyhurst and heliocentric Cartesian coordinates is

$$x=r\,\cos\Theta\,\sin\left(\Phi-\Phi_0\right), \tag{B1a}$$

$$y=r\,\sin\Theta\,\cos B_0-\cos\Theta\,\cos\left(\Phi-\Phi_0\right)\,\sin B_0, \tag{B1b}$$

$$z=r\,\sin\Theta\,\cos B_0+\cos\Theta\,\cos\left(\Phi-\Phi_0\right)\,\cos B_0, \tag{B1c}$$

where Θ and Φ are the latitude and longitude, and B_0 is the so-called solar-B angle (the latitude of the center of the solar disk as seen by the observer, and Φ_0 is the Carrington longitude of the center of the solar disk. The gradient in Stonyhurst coordinates is given by

$$\boldsymbol{\nabla}=\widehat{\boldsymbol{\Phi}}\,\frac{1}{r\,\cos\Theta}\,\partial_\Theta+\widehat{\boldsymbol{\Theta}}\,\frac{1}{r}\,\partial_r+\widehat{\boldsymbol{r}}\,\partial_r. \tag{B2}$$

The Jacobian of transformation between heliocentric Cartesian unit vectors and Stonyhurst unit vectors is then

$$\boldsymbol{\mathcal{J}} = \boldsymbol{\nabla}\left(x, y, z\right), \tag{B3a}$$

$$= \begin{pmatrix} \cos\Phi & \sin B_0 \sin\Phi & -\cos B_0 \sin\Phi \\ -\sin\Phi\sin\Theta & \cos B_0\cos\Theta + \cos\Phi\sin B_0\sin\Theta & \cos\Theta\sin B_0 - \cos B_0\cos\Phi\sin\Theta \\ \cos\Theta\sin\Phi & \cos B_0\sin\Theta - \cos\Phi\cos\Theta\sin B_0 & \cos B_0\cos\Phi\cos\Theta + \sin B_0\sin\Theta \end{pmatrix} \tag{B3b}$$

where $\boldsymbol{\mathcal{J}}$ transforms heliocentric Cartesian to Stonyhurst unit vectors and $\boldsymbol{\mathcal{J}}^{\mathrm{T}}$ vice-versa.

$$\left(\widehat{\boldsymbol{\Phi}}, \widehat{\boldsymbol{\Theta}}, \widehat{\boldsymbol{r}}\right)^{\mathrm{T}} = \boldsymbol{\mathcal{J}} \cdot \left(\widehat{\boldsymbol{x}}, \widehat{\boldsymbol{y}}, \widehat{\boldsymbol{z}}\right)^{\mathrm{T}}, \tag{B4a}$$

$$\left(\widehat{\boldsymbol{x}}, \widehat{\boldsymbol{y}}, \widehat{\boldsymbol{z}}\right)^{\mathrm{T}} = \boldsymbol{\mathcal{J}}^{\mathrm{T}} \cdot \left(\widehat{\boldsymbol{\Phi}}, \widehat{\boldsymbol{\Theta}}, \widehat{\boldsymbol{r}}\right)^{\mathrm{T}}. \tag{B4b}$$

These unit vectors can be combined with (A2) to determine the projection of the Stonyhurst unit vectors onto the LOS.

$$\widehat{\boldsymbol{\eta}}_{\mathbf{LOS}} \cdot \boldsymbol{\mathcal{J}}^{\mathrm{T}} \cdot \widehat{\boldsymbol{\Phi}} = -\cos B_0\, \sin\Phi\, \cos\theta_\rho + \left(\cos\Phi\, \sin\psi - \sin B_0\, \sin\Phi\, \cos\psi\right) \sin\theta_\rho, \tag{B5a}$$

$$\begin{aligned} \widehat{\boldsymbol{\eta}}_{\mathbf{LOS}} \cdot \boldsymbol{\mathcal{J}}^{\mathrm{T}} \cdot \widehat{\boldsymbol{\Theta}} = {} & \left(\sin B_0\, \cos\Theta - \cos B_0\, \cos\Phi\, \sin\Theta\right) \cos\theta_\rho \\ & - \left[\sin\Phi\, \sin\Theta\, \sin\psi + \left(\sin B_0\, \cos\Phi\, \sin\Theta + \cos B_0\, \cos\Theta\right) \cos\psi\right] \sin\theta_\rho \end{aligned} \tag{B5b}$$

$$\begin{aligned} \widehat{\boldsymbol{\eta}}_{\mathbf{LOS}} \cdot \boldsymbol{\mathcal{J}}^{\mathrm{T}} \cdot \widehat{\boldsymbol{r}} = {} & \left(\cos B_0\, \cos\Phi\, \cos\Theta + \sin B_0\, \sin\Theta\right) \cos\theta_\rho \\ & + \left[\sin\Phi\, \cos\Theta\, \sin\psi - \left(\cos B_0\, \sin\Theta - \sin B_0\, \cos\,\Phi\cos\Theta\right) \cos\psi\right] \sin\theta_\rho. \end{aligned} \tag{B5c}$$

C. Heliocentric Coordinates for Meridional Flows and the Convective Blue-Shift

The convective blue-shift is conventionally described in heliocentric spherical coordinates where ϱ is the angle between the point on the solar surface and the line

connecting Sun center to the observer ($\widehat{\boldsymbol{z}}$-axis).

$$x = -\, R_\odot \, \sin\varrho \, \sin\psi, \tag{C1a}$$

$$y = R_\odot \, \sin\varrho \, \cos\psi, \tag{C1b}$$

$$z = R_\odot \, \cos\varrho, \tag{C1c}$$

Equating (A1a) and (C1a) we can obtain the law sines for the relationship between the angles

$$\frac{\sin\varrho}{d} = \frac{\sin\theta_\rho}{R_\odot} = \frac{\sin\left[\pi - (\varrho + \theta_\rho)\right]}{D_\odot}, \tag{C2}$$

where the last relationship is determined from the law of sines. Rearranging we have (see pp. 174–175 in Smart 1977)

$$\sin\left(\varrho + \theta_\rho\right) = \frac{D_\odot}{R_\odot} \, \sin\theta_\rho \tag{C3a}$$

or

$$\varrho = \sin^{-1}\left(\frac{D_\odot}{R_\odot} \, \sin\theta_\rho\right) - \theta_\rho. \tag{C3b}$$

Equation (B1) and (C1) we obtain the relations between Stonyhurst and heliocentric spherical coordinates

$$\sin\Theta = \sin B_0 \, \cos\varrho + \cos B_0 \, \sin\varrho \, \cos\psi, \tag{C4a}$$

$$\cos\Theta \, \sin\Phi = -\sin\varrho \, \sin\psi, \tag{C4b}$$

$$\cos\Theta \, \cos\Phi = \cos B_0 \, \cos\varrho - \sin B_0 \, \sin\varrho \, \cos\psi. \tag{C4c}$$

D. Evaluation of Hathaway's Integral

$$G_{\mathrm{MF},\ell}\left(B_0, \varrho\right) = \frac{1}{2\,\pi} \int_0^{2\,\pi} d\psi \, \widehat{\boldsymbol{\eta}}_{\mathbf{LOS}} \cdot \boldsymbol{\mathcal{J}}^{\mathrm{T}} \cdot \widehat{\boldsymbol{\Theta}} \, \overline{\mathrm{P}}_\ell^1\left(\sin\Theta\right). \tag{D1}$$

This is a complicated integral to evaluate given that Θ and Φ must be re-expressed as functions of ϱ and ψ. Noting that the associated Legendre function may be expressed in

terms of the Legendre function of order zero ($m = 0$)

$$\mathrm{P}_\ell^m\left(x\right) = (-1)^m\ \left(1-x^2\right)^{m/2}\ \frac{d^m}{dx^m}\,\mathrm{P}_\ell\left(x\right), \tag{D2}$$

and using a Lemma for the expansion of the derivative of Legendre functions $\mathrm{P}_\ell^m\left(x\right)$ (See Garfinkel 1964)

$$\frac{d\,\mathrm{P}_\ell\left(x\right)}{dx} = \sum_{n=0}^{(\ell-1)/2}\left(2\,\ell-4\,n-1\right)\,\mathrm{P}_{\ell-1-2\,n}\left(x\right), \tag{D3}$$

the associated Legendre function of order one may be expressed as a terminating series of Legendre functions of order zero

$$\mathrm{P}_\ell^1\left(x\right) = -\sqrt{1-x^2}\ \sum_{n=0}^{(\ell-1)/2}\left(2\,\ell-4\,n-1\right)\,\mathrm{P}_{\ell-1-2\,n}\left(x\right). \tag{D4}$$

Substituting $x = \sin\Theta$

$$\mathrm{P}_\ell^1\left(\sin\Theta\right) = -\cos\Theta\ \sum_{n=0}^{(\ell-1)/2}\left(2\,\ell-4\,n-1\right)\,\mathrm{P}_{\ell-1-2\,n}\left(\sin\Theta\right), \tag{D5}$$

and using the Spherical Harmonic Addition Theorem

$$\begin{aligned}\mathrm{P}_\ell\left(\sin\Theta\right) =& \frac{4\,\pi}{2\,\ell+1}\ \sum_{m=-\ell}^{\ell} Y_\ell^m\left(B_0,\psi/2\right)\,Y_\ell^{m*}\left(\varrho,-\psi/2\right),\\ =& \frac{2}{2\,\ell+1}\ \sum_{m=-\ell}^{\ell}\overline{\mathrm{P}}_\ell^m\left(\sin B_0\right)\,\overline{\mathrm{P}}_\ell^m\left(\cos\varrho\right)\,e^{i\,m\,\psi},\end{aligned} \tag{D6}$$

this becomes

$$\mathrm{P}_\ell^1\left(\sin\Theta\right) = -2\,\cos\Theta\ \sum_{n=0}^{(\ell-1)/2}\ \sum_{m=-(\ell-1-2\,n)}^{\ell-1-2\,n}\overline{\mathrm{P}}_{\ell-1-2\,n}^m\left(\sin B_0\right)\,\overline{\mathrm{P}}_{\ell-1-2\,n}^m\left(\cos\varrho\right)\,e^{i\,m\,\psi} \tag{D7}$$

where ψ is now external to the Legendre functions. Using (6)

$$\overline{\mathrm{P}}_\ell^1\left(x\right) = -\sqrt{\frac{\left(2\,\ell+1\right)\,\left(\ell-1\right)!}{2\,\left(\ell+1\right)!}}\,\mathrm{P}_\ell^1\left(x\right), \tag{D8}$$

we obtain a form consistent with (D1)

$$\overline{\mathrm{P}}_\ell^1\left(\sin\Theta\right) = 2\,\cos\Theta\,\sqrt{\frac{\left(2\,\ell+1\right)\,\left(\ell-1\right)!}{2\,\left(\ell+1\right)!}}\ \sum_{n=0}^{(\ell-1)/2}\ \sum_{m=-(\ell-1-2\,n)}^{\ell-1-2\,n}\overline{\mathrm{P}}_{\ell-1-2\,n}^m\left(\sin B_0\right)\,\overline{\mathrm{P}}_{\ell-1-2\,n}^m\left(\cos\varrho\right)\,e^{i\,m\,\psi} \tag{D9}$$

Thus the integral may be evaluated as

$$G_{\mathrm{MF},\ell}\left(B_0,\varrho\right) = 2\sqrt{\frac{\left(2\,\ell+1\right)\,\left(\ell-1\right)!}{2\,\left(\ell+1\right)!}}\sum_{n=0}^{(\ell-1)/2}\sum_{m=-(\ell-1-2\,n)}^{\ell-1-2\,n}\overline{\mathrm{P}}^{m}_{\ell-1-2\,n}\left(\sin B_0\right)\,\overline{\mathrm{P}}^{m}_{\ell-1-2\,n}\left(\cos\varrho\right)$$
$$\times\,\left[I^{m}_{1}\left(B_0,\rho\right)\,\cos\theta_\rho - I^{m}_{2}\left(B_0,\rho\right)\,\sin\theta_\rho\right]. \tag{D10}$$

where

$$I^{m}_{1}\left(B_0,\rho\right) = \frac{1}{2\,\pi}\int_0^{2\,\pi} d\psi\, e^{i\,m\,\psi}\,\cos\Theta\,\left(\sin B_0\,\cos\Theta - \cos B_0\,\sin\Theta\,\cos\Phi\right), \tag{D11a}$$

$$I^{m}_{2}\left(B_0,\rho\right) = \frac{1}{2\,\pi}\int_0^{2\,\pi} d\psi\, e^{i\,m\,\psi}\,\cos\Theta\,\left[\sin\Theta\,\sin\Phi\,\sin\psi + \left(\sin B_0\,\sin\Theta\,\cos\Phi + \cos B_0\,\cos\Theta\right)\,\cos\psi\right].$$

Evaluating the first integral

$$\begin{aligned} I^{m}_{1}\left(B_0,\varrho\right) =& \frac{1}{2\,\pi}\int_0^{2\,\pi} d\psi\, e^{i\,m\,\psi}\,\cos\Theta\,\left(\sin B_0\,\cos\Theta - \cos B_0\,\sin\Theta\,\cos\Phi\right), \\ =& \frac{\sin\varrho}{2\,\pi}\int_0^{2\,\pi} d\psi\, e^{i\,m\,\psi}\,\left(\sin B_0\,\sin\varrho - \cos B_0\,\cos\varrho\,\cos\psi\right), \\ =& (-1)^{m+1}\,\sin\varrho\,\left[\left(2m^2-1\right)\cos\left(B_0+\varrho\right) + \cos\left(B_0-\varrho\right)\right]\,\frac{\sin\left(m\,\pi\right)}{2\pi m\left(m^2-1\right)}, \\ =& \delta_{m,0}\,\sin B_0\,\sin^2\varrho - \frac{1}{2}\,\delta_{|m|,1}\,\cos B_0\,\sin\varrho\,\cos\varrho. \end{aligned} \tag{D12a}$$

Similarly

$$I^{m}_{2}\left(B_0,\varrho\right) = \delta_{m,0}\,\sin B_0\,\sin\varrho\,\cos\varrho - \frac{1}{2}\,\delta_{|m|,1}\,\cos B_0\,\cos^2\varrho. \tag{D12b}$$

Noting that $I^{m}_{2}\left(B_0,\varrho\right) = -\cot\varrho\, I^{m}_{1}\left(B_0,\varrho\right)$

$$G_{\mathrm{MF},\ell}\left(B_0,\varrho\right) = \left(\cos\theta_\rho + \cot\varrho\,\sin\theta_\rho\right) \tag{D13}$$
$$\times\,2\sqrt{\frac{\left(2\,\ell+1\right)\,\left(\ell-1\right)!}{2\,\left(\ell+1\right)!}}\sum_{m=-1}^{1} I^{m}_{1}\left(B_0,\varrho\right)\sum_{n=0}^{(\ell-1)/2}\overline{\mathrm{P}}^{m}_{\ell-1-2\,n}\left(\sin B_0\right)\,\overline{\mathrm{P}}^{m}_{\ell-1-2\,n}\left(\cos\varrho\right).$$

Noting the symmetry property of the Legendre functions

$$\mathrm{P}^{-m}_{\ell}\left(x\right) = \left(-1\right)^{m}\,\frac{\left(\ell-m\right)!}{\left(\ell+m\right)!}\,\mathrm{P}^{m}_{\ell}\left(x\right), \tag{D14a}$$

$$\overline{\mathrm{P}}^{-m}_{\ell}\left(x\right) = \left(-1\right)^{m}\,\overline{\mathrm{P}}^{m}_{\ell}\left(x\right). \tag{D14b}$$

$$G_{\mathrm{MF},\ell}\left(B_0,\varrho\right) = \sqrt{\frac{2}{2\,\ell+1}}\,\sin\left(\varrho+\theta_\rho\right)\,\sqrt{1+2\,\ell}\,\sqrt{\frac{2\,\ell+1}{\ell\,\left(\ell+1\right)}}\times \tag{D15}$$
$$\sum_{n=0}^{(\ell-1)/2}\,\Big[\overline{\mathrm{P}}^{0}_{\ell-1-2\,n}\left(\sin B_0\right)\,\overline{\mathrm{P}}^{0}_{\ell-1-2\,n}\left(\cos\varrho\right)\,\sin B_0\,\sin\varrho$$
$$-\,\overline{\mathrm{P}}^{1}_{\ell-1-2\,n}\left(\sin B_0\right)\,\overline{\mathrm{P}}^{1}_{\ell-1-2\,n}\left(\cos\varrho\right)\,\cos B_0\,\cos\varrho\Big]\,.$$

Employing an inductive proof this generally becomes

$$G_{\mathrm{MF},0}\left(B_0,\varrho\right) = 0, \tag{D16}$$
$$G_{\mathrm{MF},1}\left(B_0,\varrho\right) = \sqrt{\frac{2}{3}}\,\sin\left(\varrho+\theta_\rho\right)\,\frac{3}{2\,\sqrt{2}}\,\sin B_0\,\sin\varrho,$$
$$= \sqrt{\frac{2}{3}}\,\sin\left(\varrho+\theta_\rho\right)\,\overline{\mathrm{P}}^{0}_{1}\left(\sin B_0\right)\,\overline{\mathrm{P}}^{1}_{1}\left(\cos\varrho\right), \tag{D17}$$
$$G_{\mathrm{MF},2}\left(B_0,\varrho\right) = \sqrt{\frac{2}{5}}\,\sin\left(\varrho+\theta_\rho\right)\,\frac{5}{8}\,\sqrt{\frac{3}{2}}\,\left[1-3\,\cos\left(2\,B_0\right)\right]\,\sin\varrho\,\cos\varrho,$$
$$= \sqrt{\frac{2}{5}}\,\sin\left(\varrho+\theta_\rho\right)\,\overline{\mathrm{P}}^{0}_{2}\left(\sin B_0\right)\,\overline{\mathrm{P}}^{1}_{2}\left(\cos\varrho\right), \tag{D18}$$

and generally

$$G_{\mathrm{MF},\ell}\left(B_0,\varrho\right) = \sqrt{\frac{2}{2\,\ell+1}}\,\sin\left(\varrho+\theta_\rho\right)\,\overline{\mathrm{P}}_{\ell}\left(\sin B_0\right)\,\overline{\mathrm{P}}^{1}_{\ell}\left(\cos\varrho\right). \tag{D19}$$

where $\theta_\rho \approx 0$ corresponds to the results of Hathaway (1992).

D.1. Karhunen-Loéve (KL) Analysis

The Karhunen-Loéve (KL) Analysis (Loéve 1955) is known by various names: Principle Component Analysis, Proper Orthogonal Decomposition, Empirical Orthogonal Functions, and/or the Hoteling transform. The approach presented here follows the Method of Snapshots (Lumley 1967; Sirovich 1987; Holmes et al. 1996). The goal of KL is to determine an optimal representation for the data – optimal in the sense that the vector **d** maximizes

the projection onto the median subtracted $\mathbb{R}^{N_\mathrm{D}\times N_t}$ image array $\boldsymbol{I}$. This optimality can be expressed by the functional

$$\mathcal{J}\left(\mathbf{d}\right) = N_\mathrm{D}^{-1}\,\mathbf{d}^\dagger\,\boldsymbol{I}^\dagger\,\boldsymbol{I}\,\mathbf{d} - \lambda\,\left(\mathbf{d}^\dagger\cdot\mathbf{d} - 1\right), \tag{D20}$$

where † represents the conjugate transpose for complex data or just the transpose for real data as is being considered here and the constraint ensures normalization. The $\mathbb{C}^{N_t\times N_t}$ spatially averaged covariance matrix of the image sequence is defined as

$$\boldsymbol{\mathcal{C}} \equiv \frac{\boldsymbol{I}^\dagger\,\boldsymbol{I}}{N_\mathrm{D}}, \tag{D21a}$$

$$\mathcal{C}_{nm} = \frac{1}{N_\mathrm{D}}\sum_{i=1}^{N_\mathrm{D}}\left[\boldsymbol{I}^\dagger\right]_{ni}\,\left[\boldsymbol{I}\right]_{im}, \tag{D21b}$$

which permits the expression of the functional

$$\mathcal{J}\left(\mathbf{d}+\delta\boldsymbol{\epsilon}\right) = \left(\mathbf{d}^\dagger+\delta\boldsymbol{\epsilon}^\dagger\right)\,\boldsymbol{\mathcal{C}}\,\left(\mathbf{d}+\delta\boldsymbol{\epsilon}\right) - \lambda\,\left[\left(\mathbf{d}^\dagger+\delta\boldsymbol{\epsilon}^\dagger\right)\,\left(\mathbf{d}+\delta\boldsymbol{\epsilon}\right) - 1\right] \tag{D22}$$

where $\delta\boldsymbol{\epsilon}$ is a small vector perturbation on $\mathbf{d}$. Using the calculus of variations, the first variation of the functional is

$$\lim_{\delta\to 0}\frac{d}{d\delta}\mathcal{J}\left(\mathbf{d}+\delta\boldsymbol{\epsilon}\right) = \boldsymbol{\epsilon}^\dagger\,\boldsymbol{\mathcal{C}}\,\mathbf{d} + \mathbf{d}^\dagger\,\boldsymbol{\mathcal{C}}\,\boldsymbol{\epsilon} - \lambda\,\left(\boldsymbol{\epsilon}^\dagger\,\mathbf{d} + \mathbf{d}^\dagger\,\boldsymbol{\epsilon}\right), \tag{D23a}$$

$$= \boldsymbol{\epsilon}^\dagger\,\left(\boldsymbol{\mathcal{C}}\,\mathbf{d} - \lambda\,\mathbf{d}\right) + \left(\mathbf{d}^\dagger\,\boldsymbol{\mathcal{C}}^\dagger - \lambda\,\mathbf{d}^\dagger\right)\,\boldsymbol{\epsilon}, \tag{D23b}$$

$$= \boldsymbol{\epsilon}^\dagger\,\left(\boldsymbol{\mathcal{C}}\,\mathbf{d} - \lambda\,\mathbf{d}\right) + \left[\boldsymbol{\epsilon}^\dagger\,\left(\boldsymbol{\mathcal{C}}\,\mathbf{d} - \lambda\,\mathbf{d}\right)\right]^\dagger. \tag{D23c}$$

Therefore, finding the vectors which maximize they projection onto the data is equivalent to finding the eigenvalues λ_k and eigenvectors $\mathbf{d}_k$ of the covariance matrix.

$$\boldsymbol{\mathcal{C}}\,\mathbf{d}_k = \mathbf{d}_k\,\lambda_k, \tag{D24a}$$

or

$$\boldsymbol{\mathcal{C}}\,\mathbf{D} = \mathbf{D}\,\boldsymbol{\Lambda}, \tag{D24b}$$

where the columns of $\mathbf{D} = (\mathbf{d}_1, \mathbf{d}_2, \ldots, \mathbf{d}_{N_t})$ are the eigenvectors of $\boldsymbol{\mathcal{C}}$ and $\boldsymbol{\Lambda}$ is a diagonal matrix of the eigenvalues in decreasing order. The covariance in (D21) is a hermitian $\boldsymbol{\mathcal{C}} = \boldsymbol{\mathcal{C}}^\dagger$ positive semi-definite matrix with non-negative eigenvalues that can be ordered by decreasing value $\lambda_1 \geq \lambda_2 \geq ... \geq \lambda_{N_t-1} \geq \lambda_{N_t} \geq 0$ with orthonormal eigenvectors[9]

$$\delta_{ij} = \mathbf{d}_i^\dagger \cdot \mathbf{d}_j, \tag{D25a}$$

$$\delta_{ij} = \sum_{n=1}^{N_t} \mathsf{D}_{ni}^* \, \mathsf{D}_{nj}, \tag{D25b}$$

$$\mathbf{I} = \mathbf{D}^\dagger \, \mathbf{D}, \tag{D25c}$$

where $\mathbf{I}$ is the identity matrix. Assuming that the image-sequence can be described by a $\mathbb{C}^{N_\mathrm{D} \times N_t}$ matrix of spatial eigenmodes $\boldsymbol{\Phi}$ and $\mathbb{C}^{N_t \times N_t}$ matrix of temporal coefficients $\boldsymbol{\alpha}$, this *ansatz* takes the form

$$\boldsymbol{I} = \boldsymbol{\Phi} \, \boldsymbol{\alpha}^\dagger, \tag{D26a}$$

$$\boldsymbol{\alpha} \equiv \mathbf{D} \, \boldsymbol{\Lambda}^{1/2}. \tag{D26b}$$

Post-multiplying (D26a) by $\mathbf{D}$ and using the orthogonality relationship (D25c)

$$\boldsymbol{I} \, \mathbf{D} = \boldsymbol{\Phi} \, \boldsymbol{\Lambda}^{1/2} \tag{D27}$$

results in the equation for the spatial eigenfunctions $\boldsymbol{\Phi}$ where

$$\boldsymbol{\Phi} \equiv \boldsymbol{I} \, \mathbf{D} \, \boldsymbol{\Lambda}^{-1/2} \tag{D28}$$

Multiplying this by its adjoint

$$\boldsymbol{\Phi}^\dagger \, \boldsymbol{\Phi} = \boldsymbol{\Lambda}^{-1/2} \, \mathbf{D}^\dagger \, \boldsymbol{I}^\dagger \, \boldsymbol{I} \, \mathbf{D} \, \boldsymbol{\Lambda}^{-1/2}, \tag{D29}$$

---

[9]Since the temporal median of each pixel is subtracted from the image sequence, the last eigenvalue λ_{N_t} will often be close to zero. Precision errors can manifest themselves as negative eigenvalues despite the positive semi-definite properties of the matrix $\boldsymbol{\mathcal{C}}$. Standard practice is to set this negative eigenvalue to zero effectively ignoring it in any modal reconstruction.

and using (D21)

$$\mathbf{\Phi}^{\dagger}\,\mathbf{\Phi} = N_{\mathrm{D}}\,\mathbf{\Lambda}^{-1/2}\,\mathbf{D}^{\dagger}\,\boldsymbol{\mathcal{C}}\,\mathbf{D}\,\mathbf{\Lambda}^{-1/2}, \tag{D30}$$

followed by (D24) produces

$$\mathbf{\Phi}^{\dagger}\,\mathbf{\Phi} = N_{\mathrm{D}}\,\mathbf{\Lambda}^{-1/2}\,\mathbf{D}^{\dagger}\,\mathbf{D}\,\mathbf{\Lambda}\,\mathbf{\Lambda}^{-1/2}, \tag{D31}$$

which by virtue of (D25c) becomes the orthogonality relationship for the spatial eigenfunctions

$$\mathbf{\Phi}^{\dagger}\,\mathbf{\Phi} = N_{\mathrm{D}}\,\mathbf{\Lambda}^{-1/2}\,\mathbf{\Lambda}\,\mathbf{\Lambda}^{-1/2} = N_{\mathrm{D}}\,\mathbf{I}. \tag{D32}$$

The temporal coefficients are orthogonal

$$\boldsymbol{\alpha}^{\dagger}\,\boldsymbol{\alpha} = \mathbf{\Lambda}, \tag{D33}$$

which implies that the temporal dynamics of the spatial eigenfunctions is on average uncorrelated. The temporal coefficients may also be used to reconstruct the covariance matrix

$$\boldsymbol{\mathcal{C}} = \boldsymbol{\alpha}\,\boldsymbol{\alpha}^{\dagger}. \tag{D34}$$

An analogous methodology could be applied to the time-averaged two-point time-averaged spatial correlation function $\boldsymbol{I}\boldsymbol{I}^{\dagger}/N_t$ instead of the spatially averaged correlation function in (D21). However, this direct method leads to an $\mathbb{C}^{N_{\mathrm{D}}\times N_{\mathrm{D}}}$ correlation matrix with $N_{\mathrm{D}} \simeq 10^7$ spatial eigenvalues and eigenvectors which is prohibitively large for present computers. The method of snapshots, described above, is a practical method to obtain similar results when $N_t \ll N_{\mathrm{D}}$ (Sirovich 1987).

REFERENCES

Beck, J. G., & Giles, P. 2005, ApJ, 621, L153

Beckers, J. M., & Nelson, G. D. 1978, Sol. Phys., 58, 243

Bjerhammar, A. 1951, Application of Calculus of Matrices to Method of Least Squares with Special Reference to Geodetic Calculations, Kungl. tekniska högskolans handlingar (Lindståhl)

Borrero, J. M., Tomczyk, S., Kubo, M., Socas-Navarro, H., Schou, J., Couvidat, S., & Bogart, R. 2009, ArXiv e-prints, submitted to *Sol. Phys.*

Cavanaugh, J. E. 1999, Statist. Probab. Lett., 42, 333

Centeno, R., Schou, J., Hayashi, K., Norton, A., Hoeksema, J. T., Liu, Y., Leka, K. D., & Barnes, G. 2014, Sol. Phys., 289, 3531

Chintzoglou, G., & Zhang, J. 2013, ApJ, 764, L3

Couvidat, S. 2014, in Solar Subsurface Flows from Helioseismology: Problems and Prospects, helioseismology Workshop, Stanford, CA, `http://hmi.stanford.edu/mtgs/workshop1407/agenda.html`

Couvidat, S., Rajaguru, S., Wachter, R., Sankarasubramanian, K., Schou, J., & Scherrer, P. 2012, Solar Physics, 278, 217

Craven, P., & Wahba, G. 1979, Numerische Mathematik, 31, 377

Emilio, M., Couvidat, S., Bush, R. I., Kuhn, J. R., & Scholl, I. F. 2015, The Astrophysical Journal, 798, 48

Garfinkel, B. 1964, AJ, 69, 567

Hathaway, D. 1988, Solar Physics, 117, 329

Hathaway, D. H. 1992, Sol. Phys., 137, 15

—. 1996, ApJ, 460, 1027

Hoeksema, J. T., Liu, Y., Hayashi, K., Sun, X., Schou, J., Couvidat, S., Norton, A., Bobra, M., Centeno, R., Leka, K. D., Barnes, G., & Turmon, M. 2014, Sol. Phys.

Högbom, J. A. 1974, A&AS, 15, 417

Holmes, P., Lumley, J. L., & Berkooz, G. 1996, Turbulence, coherent structures, dynamical systems and symmetry (Cambridge University Press)

Leka, K. D. 2011, in Astronomical Society of the Pacific Conference Series, Vol. 437, Astronomical Society of the Pacific Conference Series, ed. J. R. Kuhn, D. M. Harrington, H. Lin, S. V. Berdyugina, J. Trujillo-Bueno, S. L. Keil, & T. Rimmele, 157–+

Leka, K. D., & Barnes, G. 2012, Sol. Phys., 277, 89

Leka, K. D., Barnes, G., Crouch, A. D., Metcalf, T. R., Gary, G. A., Jing, J., & Liu, Y. 2009, Sol. Phys., 260, 83

Leka, K. D., Barnes, G., Gary, G. A., Crouch, A. D., & Liu, Y. 2012, Sol. Phys., 276, 441

Leka, K. D., & Steiner, O. 2001, ApJ, 552, 354

Liu, Y., Hoeksema, J. T., Scherrer, P. H., Schou, J., Couvidat, S., Bush, R. I., Duvall, T. L., Hayashi, K., Sun, X., & Zhao, X. 2012, Sol. Phys., 279, 295

Liu, Y., & Schuck, P. W. 2012, ApJ, 761, 105

Loéve, M. M. 1955, Probability Theory (Princeton, N.J.: VanNostrand)

Lumley, J. L. 1967, Atmospheric turbulence and wave propagation, ed. A. M. Yaglom & V. I. Tatarski (Moscow: Nauka), 166–178

Mochizuki, E. 1992, Sol. Phys., 142, 395

Moore, E. H. 1920, Bull. Amer. Math. Soc., 26, 394

Orozco Suárez, D., Bellot Rubio, L. R., Del Toro Iniesta, J. C., Tsuneta, S., Lites, B., Ichimoto, K., Katsukawa, Y., Nagata, S., Shimizu, T., Shine, R. A., Suematsu, Y., Tarbell, T. D., & Title, A. M. 2007, PASJ, 59, 837

Penrose, R. 1955, Mathematical Proceedings of the Cambridge Philosophical Society, 51, 406

Roberts, D. H., Lehar, J., & Dreher, J. W. 1987, AJ, 93, 968

Scherrer, P. H., Schou, J., Bush, R. I., Kosovichev, A. G., Bogart, R. S., Hoeksema, J. T., Liu, Y., Duvall, T. L., Zhao, J., Title, A. M., Schrijver, C. J., Tarbell, T. D., & Tomczyk, S. 2012, Sol. Phys., 275, 207

Schou, J., Scherrer, P. H., Bush, R. I., Wachter, R., Couvidat, S., Rabello-Soares, M. C., Bogart, R. S., Hoeksema, J. T., Liu, Y., Duvall, T. L., Akin, D. J., Allard, B. A., Miles, J. W., Rairden, R., Shine, R. A., Tarbell, T. D., Title, A. M., Wolfson, C. J., Elmore, D. F., Norton, A. A., & Tomczyk, S. 2012, Sol. Phys., 275, 229

Schuck, P. W. 2005, ApJ, 632, 53

—. 2006, ApJ, 646, 1358

—. 2008, ApJ, 683, 1134, http://arxiv.org/abs/0803.3472

Schuck, P. W. 2010, ApJ, 714, 68

Schwarz, G. 1978, The annals of statistics, 6, 461

Sirovich, L. 1987, Quarterly of Appl. Math., XLV, 561

Smart, W. M. 1977, Textbook on Spherical Geometry, 6th edn. (New York, NY: Cambridge University Press), revised by R. M. Green

Snodgrass, H. B. 1984, Sol. Phys., 94, 13

Tange, O. 2011, ;login: The USENIX Magazine, 36, 42

Thompson, W. T. 2006, A&A, 449, 791

Vemareddy, P. 2015, The Astrophysical Journal, 806, 245

Wahba, G. 1980, Ill-posed problems: numerical and statistical methods for mildly, moderately and severely ill-posed problems with noisy data, Tech. Rep. 595, Department of Statistics, University of Wisconsin

Woltring, H. J. 1986, Advances in Engineering Software and Workstations, 8, 104, 15

Ye, M., Meyer, P. D., & Neuman, S. P. 2008, Water Resources Research, 44

This manuscript was prepared with the AAS LaTeX macros v5.2.